

Theta13 Oscillation Analysis

**Dan Dwyer^b, Jiajie Ling^a, Xin Qian^b, Raymond Tsang^b, Wei Wang^c, Fenfang Wu^b,
Chao Zhang^{a*}**

^aBrookhaven National Laboratory

^bCalifornia Institute of Technology

^cCollege of William and Mary

Email: chao@bnl.gov

ABSTRACT: In this tech-note, details of the BCW theta13 oscillation analysis are presented. Anti-neutrino candidate selection rules are described. The efficiency and remaining background are estimated. The expected signal is calculated. Anti-neutrino disappearance is observed at far detectors and rate only analysis is performed to measure θ_{13} under the oscillation hypothesis.

KEYWORDS: Reactor anti-neutrino; Daya Bay; Theta13; Oscillation; Disappearance;.

*Corresponding Author

Contents

1. Anti-neutrino Candidate Selection	2
1.1 Run Selection and DAQ Live Time	2
1.2 Prompt and Delayed Energy Cut	2
1.3 Time Correlation Cut	5
1.4 Flasher Cut	6
1.5 Muon Veto Cut	7
1.6 Multiplicity Cut	8
1.7 Modified Multiplicity Cut	10
1.8 Summary of Efficiency of Cuts	11
1.9 Final Sample of Anti-neutrino Candidates	12
2. Background Estimation	16
2.1 Accidental Coincidence	16
2.2 ${}^9\text{Li}/{}^8\text{He}$	19
2.3 Fast Neutrons	21
2.4 Correlated ${}^{241}\text{Am}{}^{13}\text{C}$ Background	23
2.5 ${}^{13}\text{C}(\alpha, n){}^{16}\text{O}$ Background	23
2.6 Summary of Background Estimation	24
3. Signal Estimation	25
3.1 Target Protons	25
3.2 Reactor Anti-neutrino Flux	25
3.3 Summary of Signal Estimation	28
3.4 Absolute Flux Measurement	29
4. Theta13 Analysis and Results	31
4.1 Rate-only χ^2 Model Definition	31
4.2 Best Fit Parameters	32
4.3 Results on Theta13	33

1. Anti-neutrino Candidate Selection

In order to efficiently select the real $\bar{\nu}_e$ events and reject irrelevant background events, selection rules for $\bar{\nu}_e$ candidate events are defined as follows:

- The event must be from a good quality run period
- $0.7\text{MeV} < E_p < 12\text{MeV}$
- $6\text{MeV} < E_d < 12\text{MeV}$
- $1\mu s < \Delta T_{p-d} < 200\mu s$
- The event must pass the flasher cut
- The event must pass the muon veto cut
- The event must pass the decoupled multiplicity cut (DMC) cut

The definitions and efficiencies of these analysis cuts will be discussed in detail in the following subsections. The remaining background events after the selection will be discussed in section 2.

1.1 Run Selection and DAQ Live Time

The θ_{13} oscillation analysis selects data from Dec 24, 2011 to Feb 27, 2012, in which only runs that have all three experimental sites (Daya Bay / Ling Ao / Far) simultaneously running are used. Data quality is carefully checked to remove ‘bad’ periods, which could be caused by high voltage failures, abnormal DAQ errors, unstable event rate, unusual noisy periods, etc. The details of the data quality check is documented in doc:7464 [1]. Some runs are specially taken only to understand the properties and status of the detector, such as calibration runs and diagnostic runs. Data from these runs are not included in the oscillation analysis. The DAQ live time is then calculated by adding up the data taking time from all the clean periods, minus the short trigger disable gaps when the data flow rate is too high. The total DAQ live time is summarized in Table 5.

In addition, due to the early commissioning and large statistics, near site AD1 and AD2 data from Sept 23, 2011 to Dec 23, 2011 are specially used to understand and compare the performance of the detectors. This period is also unblinded so that an absolute measurement of reactor flux can be made. This period is however not used for θ_{13} oscillation analysis due to the lack of far site running.

1.2 Prompt and Delayed Energy Cut

The energy reconstruction algorithm used in this analysis is *AdSimple*. The details of this algorithm is documented in doc:7334 [2]. The following cuts on the visible energy of prompt and delayed events are applied:

- $0.7\text{MeV} < E_p < 12\text{MeV}$
- $6\text{MeV} < E_d < 12\text{MeV}$

Given the reactor antineutrino spectrum and the detector resolution, the prompt visible energy cut selects the positron signal from the IBD interaction with close to 100% efficiency and negligible errors. From simulation (doc:7548 [4]), this efficiency is 99.88%. The trigger efficiency at normal DAQ threshold is effectively 100% with negligible errors above 0.7 MeV visible energy [3]. Fig 9(a) shows the distribution of prompt energy of IBD interaction at near sites and far site.

The delayed visible energy cut selects the neutron signals from IBD interaction. The Daya Bay Gd-LS is 0.1% Gd by weight such that about 85% of the neutrons will be captured by a gadolinium atom with the remaining 15% captured by hydrogen. The neutron capture on hydrogen releases a single gamma particle of 2.2 MeV, so this signal is excluded by the delayed energy cut. Due to the relatively high energy nGd peak (8 MeV) that is above most of the radioactive background, the accidental coincidence background is relatively low and no fiducial volume cut is required. The analysis thus is not dependent on the event vertex reconstruction, which usually contribute to the largest systematic uncertainties.

The total number of IBD interactions is determined by the total number of target protons in the GdLS (target volume). However, two corrections are needed. Some IBD neutrons near the edge of the GdLS acrylic vessel can transport out to the LS region, then they can only capture on hydrogen. This is called ‘spill-out’ effect. From simulation (doc:7686 [5]), including ‘spill-out’ effect, the efficiency of only selecting neutron capture on Gd is $83.83\% \pm 0.69\%$. On the other hand, neutrons from IBD interactions outside of the GdLS region, such as in inner acrylic vessel and in LS can transport into the GdLS region and capture on Gd. This is called ‘spill-in’ effect. From simulation (doc:7686 [5]), the ‘spill-in’ effect increases the detection rate by $5.03\% \pm 0.10\%$.

When a neutron is captured by Gd, it has a 0.1848 probability of being captured by ^{155}Gd releasing gammas with a total energy of 8.536 MeV, and a 0.8151 probability of being captured by ^{157}Gd , releasing 7.937 MeV. Contributions from other Gd isotopes can be ignored. The mean capture peak, taken as the average of the two peaks weighted by their neutron capture probability, is 8.047 MeV. Fig. 9(b) shows the distribution of delayed energy of IBD interaction in one of the

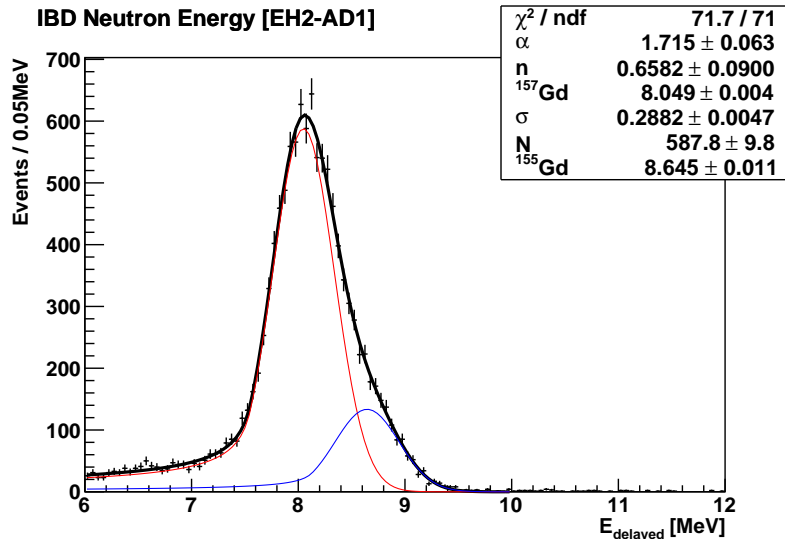


Figure 1. IBD delayed energy distribution in EH2-AD1, fitted with sum of two crystal ball functions.

ADs. The tail at low energy end of the peak is caused by events near the edge of the IAV whose gammas escape the scintillation region. Sum of two crystal ball functions (representing the two Gd isotope capture gammas) is used to model such an energy loss mechanism. The crystal ball function is defined in Eqn 1.1.

$$f(x; \alpha, n, \bar{x}, \sigma) = N \cdot \begin{cases} e^{-\frac{(x-\bar{x})^2}{2\sigma^2}}, & \frac{x-\bar{x}}{\sigma} > -\alpha \\ A \cdot (B - \frac{x-\bar{x}}{\sigma})^{-n}, & \frac{x-\bar{x}}{\sigma} \leq -\alpha \end{cases}$$

$$A = \left(\frac{n}{|\alpha|}\right)^n \cdot e^{-\frac{|\alpha|^2}{2}}, \quad B = \frac{n}{|\alpha|} - |\alpha| \quad (1.1)$$

To improve the robustness of the fit and to reflect the physics process, constraint has been enforced such that α, n are the same in the two crystal ball functions, and $N_1/N_2, \sigma_1/\sigma_2$ are fixed according to the capture ratio and energy resolution of the two peaks. An example fit result is shown in Fig 1.

From simulation (doc:7548 [4]), the absolute efficiency of delayed visible energy cut is 90.71%. Fig. 2 shows the IBD delayed energy shape comparison between data and MC. In MC, only true neutron capture on Gd events are shown. In data, we require prompt energy higher than 4 MeV to suppress the accidental background. As can be seen in Fig 2(a), the simulation does not exactly match the data, mainly due to the un-tuned energy scale and resolution. After tuning the MC and data to match the shape (Fig. 2(b), doc:7682 [7]), the the absolute efficiency of delayed visible energy cut is estimated to be $92.24\% \pm 0.51\%$. With the same tuning, the prompt energy cut efficiency is brought up to $99.90\% \pm 0.10\%$.

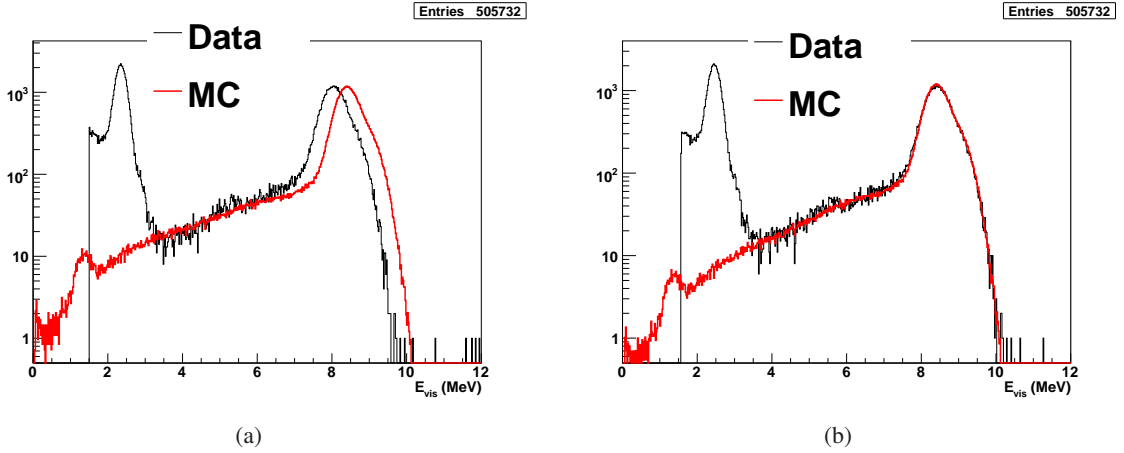


Figure 2. IBD delayed energy shape comparison between data and MC (a) before any tuning. (b) after tuning the MC and data to match. In Data, we require $E_p > 4$ MeV to suppress the accidental background. In MC, only true neutron capture on Gd events are shown.

Various data sample that have specific energy peaks are selected to study the energy scale uncertainties between ADs, including IBD neutrons, spallation neutrons, ^{241}Am , ^{13}C , ^{60}Co , ^{68}Ge sources at different positions, radioactivity peaks from ^{208}Tl (gamma), ^{40}K (gamma), ^{210}Po (alpha), and alpha's from ^{212}Po , ^{214}Po , ^{215}Po selected from Bi-Po beta-alpha coincidence decays. The results are summarized in doc:7518 [6]. The full volume energy scale uncertainty is estimated to be 0.7% at 6 MeV, translating into 0.18% uncertainty in the delayed energy cut [8]. Adding the

tail shape uncertainty 0.19% (doc:7682 [7]), the total relative uncertainty between detectors of the delayed energy cut is estimated to be 0.26%.

1.3 Time Correlation Cut

The temporal correlation between the prompt and delayed event from the inverse beta decay is a very powerful tool to reject background from the $\bar{\nu}_e$ events. The following selection rule on the time correlation is applied in this analysis:

- $1\mu s < \Delta T_{p-d} < 200\mu s$

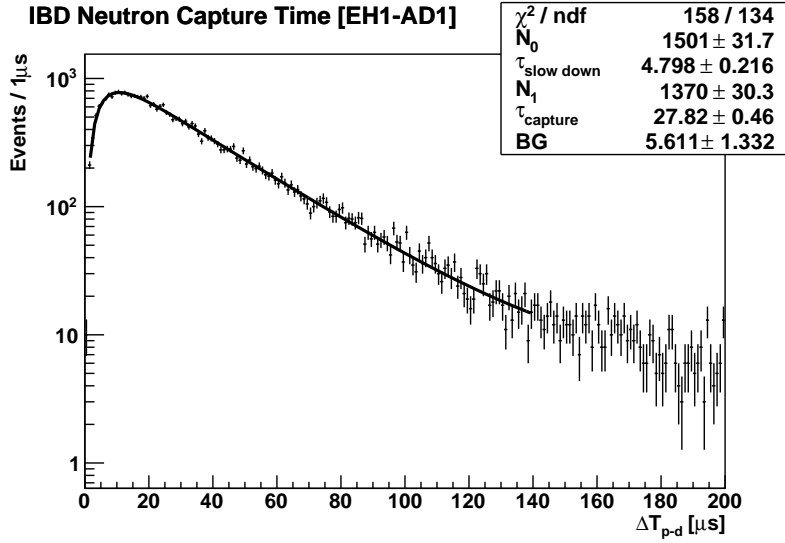


Figure 3. Time between prompt and delayed events in anti-neutrino candidates

Fig. 3 shows the distribution of time between prompt and delayed events in one of the ADs. The distribution can be characterized by an initial rising component caused by neutron thermalization and a later decaying component caused by neutron capture. The probability of a thermalized neutron get captured in a time interval dt is constant over time (“lack of aging”), thus the neutron capture time follows an exponential distribution. Near thermal energy, the neutron capture cross section is approximately inversely proportional to its velocity, so the mean capture time is independent of the neutron energy. However, it takes about $8\mu s$ to slow down a 10 keV neutron (from IBD interaction) to thermal energy, mainly by elastic scattering on hydrogen, during which the the neutron capture cross section has a complicated form [26]. We can model the mechanism during the the initial thermalization period by introducing a negative decay component in the Δt distribution (doc:7299 [9]):

$$N(t) = -N_0 e^{-t/t_0} + N_1 e^{-t/t_1} + N_{bg} \quad (1.2)$$

where t_0 and t_1 represents the characteristic time of the neutron thermalization time and neutron capture time, and N_{bg} represents the flat background components that have no temporal correlation. An example fit result is shown in Fig 3. Alternatively, we fit the capture time spectrum with a single exponential decay plus a flat background, but limiting the fitting range starting from $20\mu s$, to avoid the initial thermalization period. The two methods give similar results.

It should be noted that the fitted neutron capture time above is an “effective” capture time, because for events at the edge of the IAV, spill-in neutrons spend more time in the LS region which effectively increases the neutron capture time. By limiting the events to be within the center of the detector, we can get a fitting result closer to the “true” capture time. Such study has been done for IBD neutrons, spallation neutrons and AmC neutrons (doc:7672 [10]), the results are summarized in table 1. The observed IBD neutron capture time difference between ADs is 0.5% which translates

Table 1. Summary of the neutron capture time study from different neutron samples

	AD1	AD2	AD3	AD4	AD5	AD6
IBD	27.8 ± 0.4	28.5 ± 0.4	27.7 ± 0.4	25.0 ± 1.3	28.3 ± 1.3	28.5 ± 1.3
Spallation	28.4 ± 0.1	28.4 ± 0.1	28.9 ± 0.2	26.6 ± 0.8	27.8 ± 0.9	26.2 ± 0.8
$^{242}\text{Am}^{13}\text{C}$	28.3 ± 0.2	28.5 ± 0.2	28.0 ± 0.3	28.6 ± 0.2	27.5 ± 0.2	28.1 ± 0.2

into 0.1% relative uncertainty in determining the fraction of IBD neutrons capture on Gd.

The IBDs that have prompt and delayed events happen within $1\mu\text{s}$ are excluded to decouple from the trigger electronics effects, for example, if both prompt and delayed events happened within the trigger time window. From simulation (doc:7686 [5]), the absolute efficiency from the Δt cut is 98.57%. The inefficiency is dominantly by the tail of the capture distribution from spill-in neutrons. The inefficiency from neutron capture within $1\mu\text{s}$ is only 0.2%. Fig. 4 shows the IBD neutron capture time comparison between data and MC at the center of AD (Fig. 4(a)) and inside full GdLS volume (Fig. 4(b)). At the center, they match very well. For the full volume,

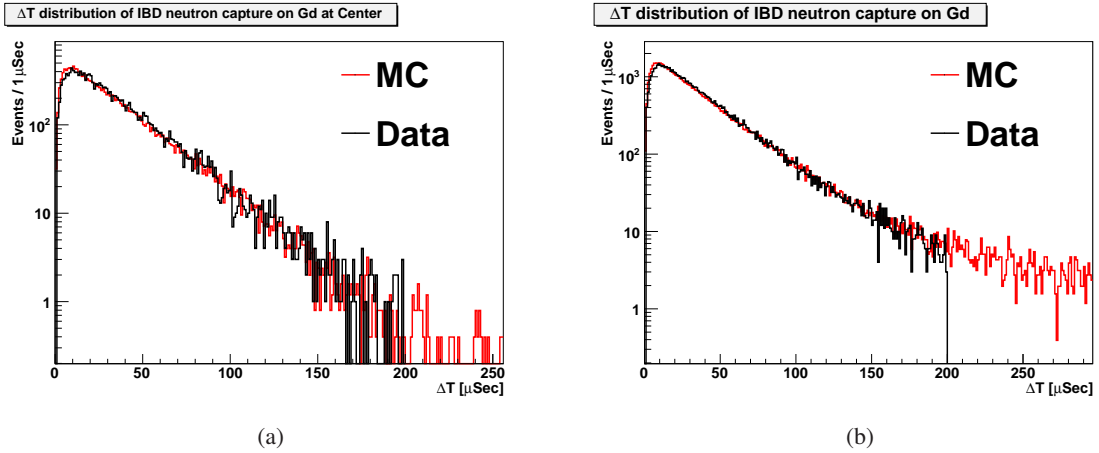


Figure 4. IBD neutron capture time comparison between data and MC (a) at the center of AD (b) Full GdLS volume.

the tail shape is somewhat different. By comparing the the data with MC and between ADs, the correlated and uncorrelated uncertainty of the capture time cut efficiency is determined to be 0.19% and 0.02%, respectively.

1.4 Flasher Cut

About 5% of the AD events are so-called flasher events, instrumental background events resulting from an electronic discharge in the dynode of a PMT. About 5% of the PMTs have been identified

as sources of flasher events. The observed energy of flasher events ranges from threshold to 100 MeV, and flasher rate in the energy range (6 MeV, 12 MeV) is around 0.7 Hz . Such a high rate of neutron-like events causes large accidental background contributions (80% compared with anti-neutrino rate), thus flasher events need to be suppressed. The flasher events have a specific charge and timing pattern that is distinct from other physical events. As such, they can be easily identified and removed. The flasher identification algorithm is documented in doc:7434 [11]. Both the prompt and delayed events are required to pass the flasher cut. The efficiency of flasher cut on the true IBD events is estimated to be 0.9993 (doc:7677 [12]). The possible remaining correlated flashers from the inefficiency of the flasher cut on flasher events, which can not be subtracted from the accidentals, is studied in doc:7537 [13] and is negligible.

1.5 Muon Veto Cut

Cosmic muons entering the detectors produce large amount of spallation products. Among them the spallation neutrons and the spallation ^9Li / ^8He could give prompt-delayed signals and mimic the $\bar{\nu}_e$ events. The high energy spallation neutrons predominantly lose energies by elastically scattering on ^1H nuclei. The recoiled protons inside the liquid scintillator could give prompt signals while the thermalized neutrons capture on gadolinium give delayed signals. It is also possible that a pair of neutron captures will coincide in time given that the neutrons are essentially created at the same time, which also fakes an $\bar{\nu}_e$ event. To remove those spallation neutrons the following muon veto cuts are applied:

- AD is vetoed $2\ \mu\text{s}$ before any muons that are tagged by Water Pool or the same AD.
- AD is vetoed $200\ \mu\text{s}$ after muons that are tagged by Water Pool.
- AD is vetoed $1000\ \mu\text{s}$ after muons that are tagged by the same AD.

where the muon tagging for Water Pool and AD is defined as:

- *Water Pool Muon*: Number of *Inner Water Pool* hit pmt channel > 12 in or number of *Outer Water Pool* hit pmt channel > 12
- *AD Muon*: The total light yield in the AD > 3000 photoelectrons (PE)

Due to the imperfect trigger time alignment between AD and Water Pool electronics, there could be latency up to $2\ \mu\text{s}$ between the two sub-detector system. That's why we require a veto of $2\ \mu\text{s}$ before a muon which may not seem obvious to the readers. In addition, as will be discussed in the next section, in order to decouple the muon veto efficiency from the multiplicity cut efficiency calculation, an additional $400\ \mu\text{s}$ veto after a muon is added to the previous veto criteria ¹ The effective muon veto time that is used in this analysis then becomes:

- AD is vetoed $2\ \mu\text{s}$ before any muons that are tagged by Water Pool or the same AD.

¹In the original DMC, we also require an additional $200\ \mu\text{s}$ veto before the muon. Due to an electronic noise in the water system which is correlated with IBD event, this requirement is removed in this study (*partial DMC*). Details will be discussed in section 1.7

- AD is vetoed 600 μs after muons that are tagged by Water Pool.
- AD is vetoed 1400 μs after muons that are tagged by the same AD.

Since the neutron capture time in Gd-LS is only $\sim 30\mu s$, the muon veto essentially removes all the correlated spallation neutron background after tagged muons. The remaining fast neutron background after untagged muons will be discussed in Section 2.3. The muon veto also removes the short post-muon noisy period due to the electronic effects, typically less than $10\mu s$.

The spallation ${}^9\text{Li}$ beta decays ($\tau_{1/2} = 178.3\text{ms}$, $Q = 13.6\text{MeV}$) to ${}^9\text{Be}$ and the beta particle gives a prompt signal. The excited states of ${}^9\text{Be}$ however are neutron unstable and could decay to ${}^8\text{Be}$ with emitting a neutron. This neutron then thermalizes, captures on gadolinium and gives a delayed signal. A similar mechanism exists for spallation ${}^8\text{He}$ ($\tau_{1/2} = 118.5\text{ms}$, $Q = 10.7\text{MeV}$). The beta particles are not as penetrating as fast neutrons thus the ${}^9\text{Li}$ events are predominantly produced by muons traversing the scintillator. Due to the long decay time of ${}^9\text{Li}$, a long veto is needed effectively reduce this background. Given the AD muon rate of $\sim 22\text{ Hz}$, vetoing the AD after every AD muon will significantly reduce the live time of the experiment. However, as will be discussed in section 2.2, the majority of the ${}^9\text{Li}$'s are produced by a subset of AD muons that deposit more energy than MIP particles. This subset of AD muons are called AD shower muons, which is defined as:

- *AD Shower Muon*: The total light yield in the AD $> 3 \times 10^5$ photoelectrons (PE)

The following shower muon veto is applied to reduce the ${}^9\text{Li} / {}^8\text{He}$ background:

- AD is vetoed 0.4 seconds after *Shower Muons* in the same AD.

The remaining number of ${}^9\text{Li} / {}^8\text{He}$ background events after these cuts will be discussed in section 2.2.

It should be emphasized that the muon veto cut is only applied relative to the delayed event, not to the prompt event. This ensures that the veto time is independent of the neutron capture time and can be calculated accurately by counting every tagged muon and adding up the muon veto time. The loss of live time due to the muon veto is treated as an efficiency of the $\bar{\nu}_e$ selection, and is summarized in table 3. The efficiency difference in the three sites represents the different muon rate at each site, caused by the different rock overburden.

The signal efficiency from muon veto cut as a function of time is shown in Fig 5

1.6 Multiplicity Cut

After applying all above cuts, the remaining candidates are mostly true IBD events. However there is still one caveat. The IBD interaction itself only produces one pair of prompt (positron) and delayed (neutron) events, but if one or more random AD events happen coincident in time with the $\bar{\nu}_e$ event, two or more prompt-delayed pairs can be formed. An example of such case is shown in Fig. 6, where event group (1, 2) and (2, 3) are both valid IBD candidates, but only (2, 3) is the true IBD pair. Including the fake candidates will bias the energy and neutron capture time distribution, as well as the event counting (events could be double counted). A multiplicity cut is needed to remove such cases.

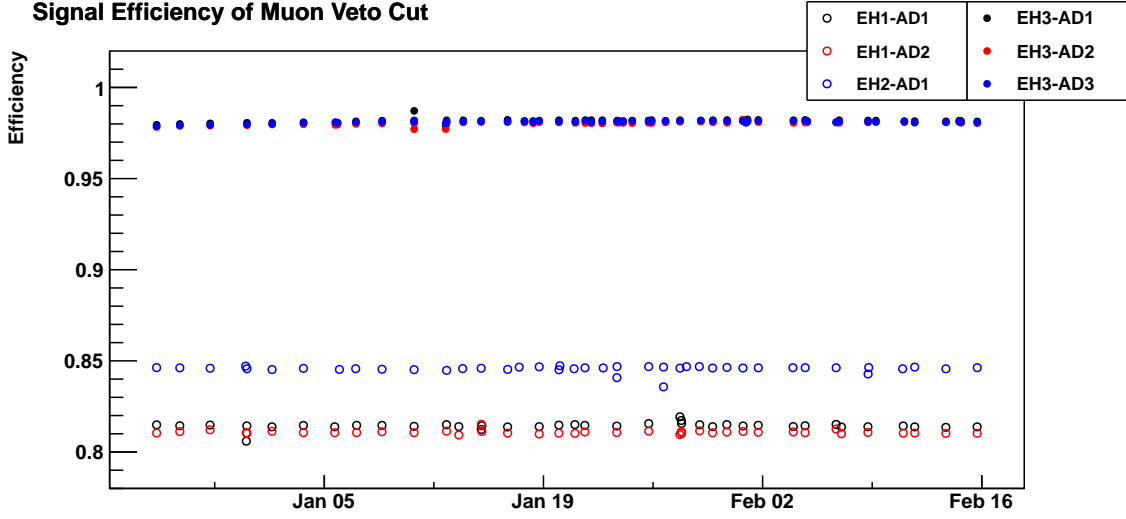


Figure 5. Signal efficiency of muon veto cut as a function of time

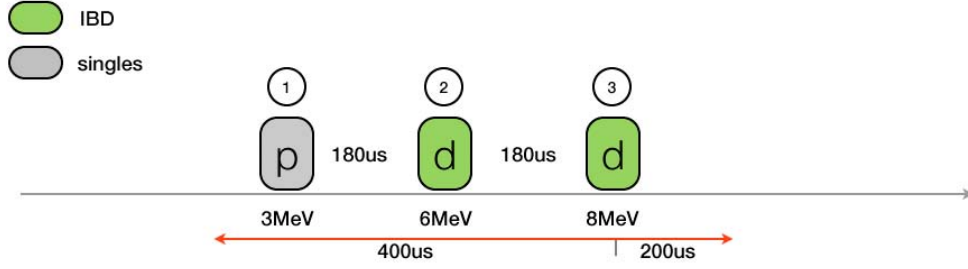


Figure 6. Illustration of Decoupled Multiplicity Cut

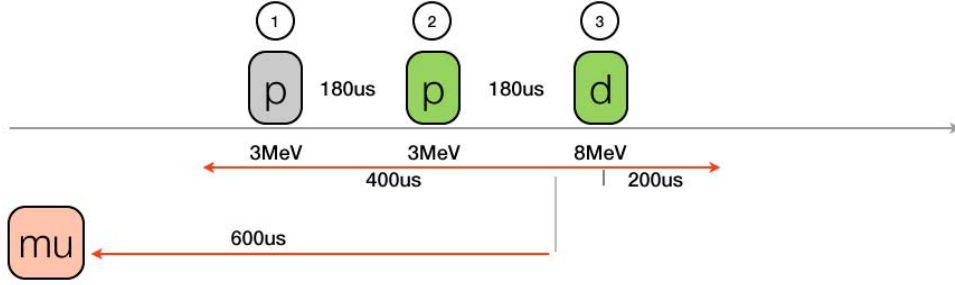


Figure 7. Illustration of Decoupled Multiplicity Cut Relation to Muons

One traditional multiplicity cut is to remove any event groups such that more than one prompt-delayed pair can be formed. The method, however, suffers from the difficulty in calculating the efficiency of the cut, because the efficiency is coupled with the neutron capture time and anti-neutrino energy. To avoid such complications, we introduce the *Decoupled Multiplicity Cut* (DMC), which is applied *after all other cuts have been applied*. DMC is defined as follows:

- Only one prompt candidate within $200\mu s$ before the delayed candidate

- No other prompt candidate within $400\mu s$ before the delayed candidate
- No delayed candidate within $200\mu s$ after the delayed candidate

In the previous example Fig. 6, candidate (1, 2) is removed by item 3 and candidate (2, 3) is removed by item 2. The efficiency of the DMC selection can be trivially calculated by $P(0; R_p \cdot 400\mu s) \cdot P(0; R_d \cdot 200\mu s)$, where $P(k; \lambda) = \lambda^k e^{-\lambda} / k!$ is the pdf of Poisson distribution of observing n events when expecting ν events. R_p and R_d is the singles rate of prompt-like events and delayed-like events, which can be calculated accurately on a run-by-run basis that is discussed in section 2.1. Since R_p is on the order of ~ 70 Hz and R_d is on the order of a thousand events per day, the DMC selection efficiency can be well approximated with $1 - R_p \cdot 400\mu s - R_d \cdot 200\mu s$, and is summarized in table 3.

One needs to be careful when apply DMC to the events near the edge of muon veto window. An illustration is shown in Fig 7. If the muon veto window is not long enough, the DMC could cut into the region that is close to a muon, where the R_p or R_d can not be assumed to follow the singles distribution. The efficiency calculation is then coupled with the muon veto definition. In order to decouple from such situation, an additional veto of $200\mu s$ before a muon and $400\mu s$ after a muon is added to any muon veto criteria, as stated in section 1.5

The signal efficiency of multiplicity cut as a function of time is shown in Fig 8. The changes of efficiency is largely due to the changes of the R_p , the prompt-like singles rate in the AD. This will be further discussed in section 2.1 when we estimate the accidental backgrounds.

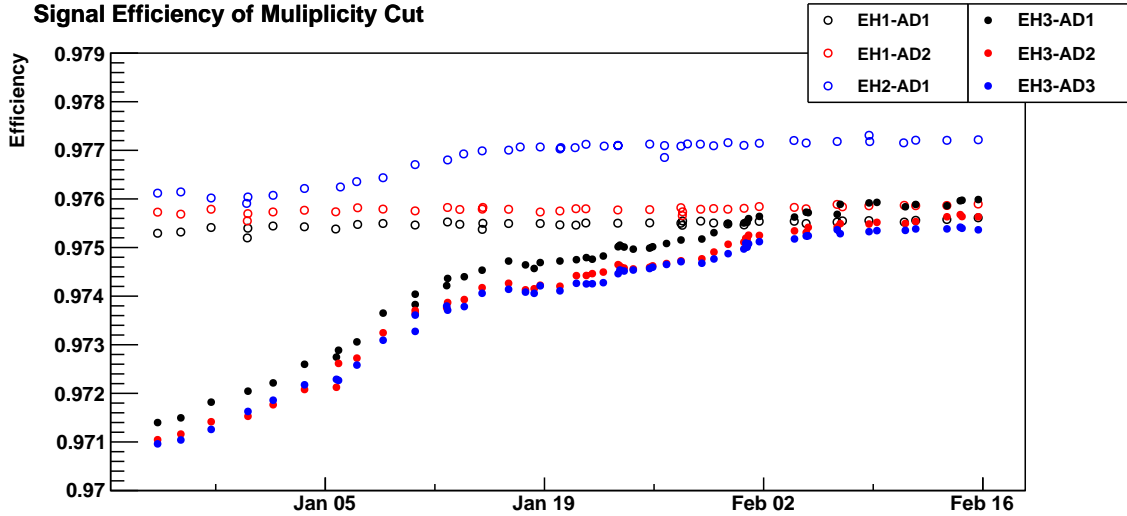


Figure 8. Signal efficiency of multiplicity cut as a function of time.

1.7 Modified Multiplicity Cut

It turns out that the *Decoupled Multiplicity Cut* needs to be modified to accommodate an unexpected electronic noise introduced by the cross-trigger from AD to Water Pool system. The cross trigger is issued by the MTB when a correlated signal, such as an IBD event, is seen by the AD.

the water system then ‘look back’ and record FEE data in the past 200 μs . The cross trigger itself can be identified by the trigger type, but it generates a noise after $\sim 100 \mu s$ in the WP FEE system which looks like a normal trigger. Sometimes the noise trigger even crosses the analysis muon threshold of $NHIT > 12$. One (crucial) assumption of the muon veto is that IBD events have no correlation with muons, so any muon veto can be treated as a live time correction. However, about 1% of the IBD events are associated with this kind of the ‘fake muon’ triggers. The original DMC vetoes 200 μs before any muons. For these correlated ‘fake muons’, DMC then removes the associated IBDs without correcting the efficiencies. In principle, such electronic noise can be identified by looking at the charge patterns, etc. Before such noise ID algorithm is fully developed and studied, we decide to modify the DMC as follows (*partial DMC*) to work around this issue:

- On muon veto cuts: remove the extra 200 μs veto before a muon. Now it becomes
 - AD is vetoed 2 μs before any muons that are tagged by Water Pool or the same AD.
 - AD is vetoed 600 μs after muons that are tagged by Water Pool.
 - AD is vetoed 1400 μs after muons that are tagged by the same AD.
 - AD is vetoed 0.4 seconds after *Shower Muons* in the same AD.
- On multiplicity cuts: require outside of the muon veto window, no delayed candidate within 200 μs after the delayed candidate. Now it becomes
 - Only one prompt candidate within 200 μs before the delayed candidate
 - No other prompt candidate within 400 μs before the delayed candidate
 - Outside of the muon veto window, no delayed candidate within 200 μs after the delayed candidate

This change has negligible impact on DMC efficiency ($< 1e-5$), since the delayed-like signal outside of muon veto window is only about 1000/day. It brings back 200 μs analysis live time for each muon.

We still prefer DMC (mathematically) if the cross trigger noise can be resolved in the future, since the calculation is then exact. The solution can be either from hardware by suppressing the noise or entirely disabling the cross trigger, or from software by develop algorithms to identify these noise triggers with high efficiency.

1.8 Summary of Efficiency of Cuts

We summarize the efficiency of the anti-neutrino candidate selection in two tables. Table 2 summarizes the common efficiencies that can apply to all ADs. For each efficiency, we quote an absolute uncertainty that is correlated among all ADs, and a relative uncertainty that is uncorrelated among ADs. The absolute efficiency and uncertainty affects all ADs in a correlated way, so it only impact the overall rate normalization. In certain analysis such as reactor flux measurements it is important to pin down the uncertainty on absolute efficiency. In theta13 relative rate analysis the precise knowledge of absolute efficiency is less important. We can even entirely remove this uncertainty from the χ^2 definition, without degrading much on the θ_{13} results. Further, as it turns out in the

Table 2. Summary of efficiency of cuts common to all ADs

Description	Efficiency	Uncertainty	
		Correlated	Uncorrelated
Gd capture ratio	0.8383	0.0060	0.10%
Spill in	1.0503	0.0010	0.02%
Delayed energy cut	0.9224	0.0051	0.26%
Prompt energy cut	0.9990	0.0010	0.01%
Capture time cut	0.9857	0.0019	0.02%
Flasher cut	0.9991	0.0002	0.01%
Total	0.7990	0.94%	0.28%

next section, the total AD correlated uncertainty is dominated by the correlated reactor flux and neutrino spectra uncertainty (about 3.1%), not by the analysis cuts.

Table 3 summarizes the efficiencies that are different among ADs. These efficiencies are also time dependent, and are calculated precisely on a run-by-run basis. The mean efficiencies weighted by the live-time of each run are shown. The uncertainties on them are negligible.

Table 3. Summary of live-time weighted mean efficiency of cuts (different among ADs)

	Daya Bay		Ling Ao	Far		
	AD1	AD2	AD1	AD1	AD2	AD3
Muon veto cut	0.8143	0.8108	0.8460	0.9815	0.9803	0.9809
Multiplicity cut	0.9755	0.9758	0.9768	0.9743	0.9739	0.9738

Combining the two tables, Table 4 summarizes the total efficiency on the IBD rate (the total IBD interaction inside the GdLS target volume) from analysis cuts.

Table 4. Summary of total efficiency on the IBD rate from analysis cuts

	Daya Bay		Ling Ao	Far		
	AD1	AD2	AD1	AD1	AD2	AD3
Total efficiency of cuts	0.6376	0.6350	0.6633	0.7675	0.7663	0.7667

1.9 Final Sample of Anti-neutrino Candidates

Table 5 summarizes the total number of $\bar{\nu}_e$ candidates observed in each AD, after the analysis cuts. Each AD at the far site sees about 3500 IBD events. The total statistical uncertainty combining the 3 ADs at the far site reaches below 1%.

We show some characteristic distributions of the $\bar{\nu}_e$ candidates in Fig 9, where events from ADs at near sites (EH1, EH2) are combined and events from ADs at the far site (EH3) are combined. The distribution in the near sites are normalized according to the far site, to emphasize the overall shape difference between the distributions. The estimated background events are not subtracted from the distributions, which causes the main shape differences between near and far

Table 5. Summary of Anti-neutrino Candidates

	Daya Bay		Ling Ao	Far		
	AD1	AD2	AD1	AD1	AD2	AD3
DAQ live time [days]	49.5527	49.5527	49.4968	48.9453	48.9453	48.9453
Number of $\bar{\nu}_e$ candidates	28692	28857	22169	3536	3464	3461

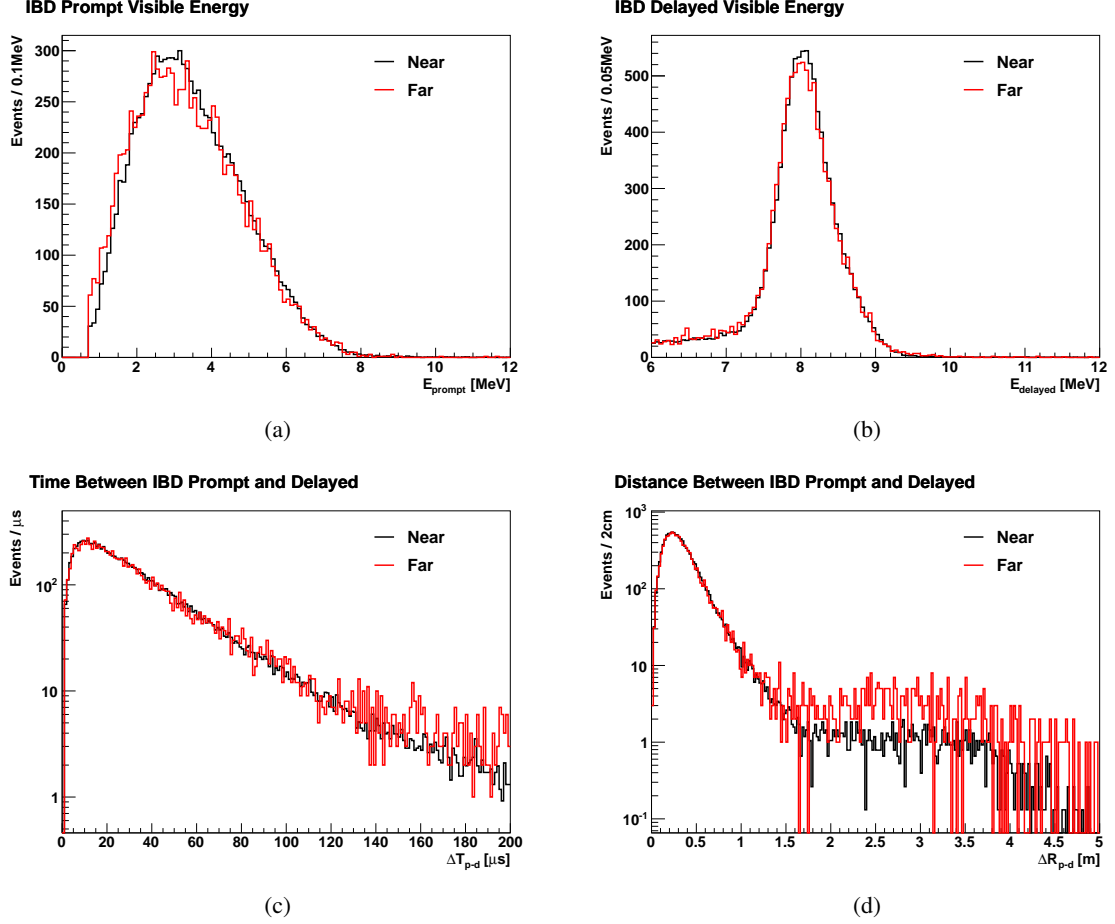


Figure 9. Some characteristic distributions of the $\bar{\nu}_e$ candidates, where events from ADs in near sites (EH1, EH2) are combined and events from ADs in far sites (EH3) are combined. The distribution in the near sites are normalized to counts in the far site, to emphasize the overall shape difference between the distributions. (a) Prompt energy spectra; (b) Delayed energy spectra; (c) Time between prompt and delayed event; (d) Distance between prompt and delayed event. The difference between the near and far distribution is mainly caused by the background events, in particular dominated by accidentals, which are not subtracted in these figures.

sites shown in the figures. As will be discussed in section 2, the dominant background are the accidentals which are concentrated at low prompt energy and have no temporal or spacial correlations between the prompt and delayed events.

Even though we do not require fiducial volume cuts in the $\bar{\nu}_e$ selection, we show the recon-

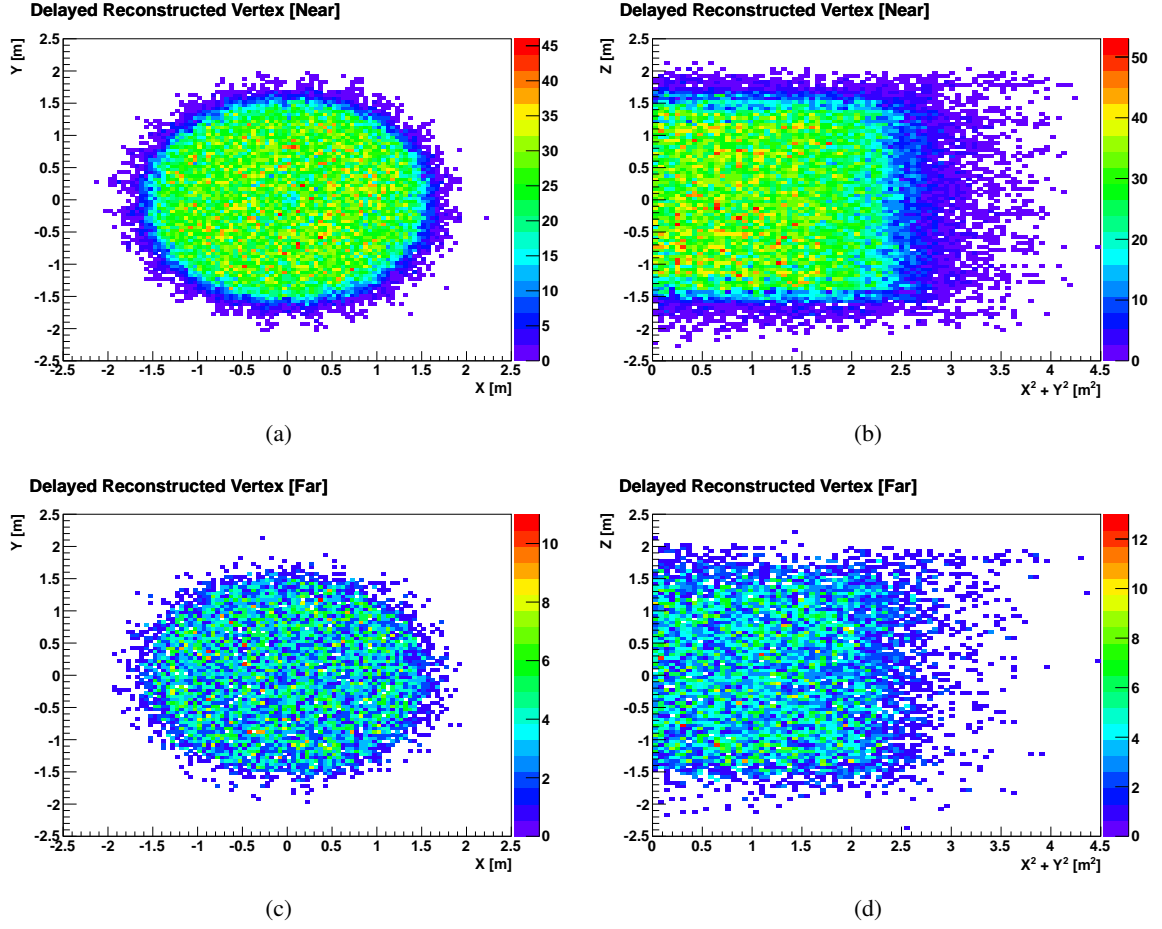


Figure 10. Reconstructed vertex distributions of the $\bar{\nu}_e$ candidates, where events from ADs in near sites (EH1, EH2) are combined and events from ADs in far sites (EH3) are combined. (a) (b) Near site; (c) (d) Far Site. Delayed energy spectra; (c) Time between prompt and delayed event; The events outside of the GdLS volume are largely due to the accidental background events.

structed vertex distributions of the $\bar{\nu}_e$ candidates in Fig 10, where events from ADs in near sites (EH1, EH2) are combined and events from ADs in far sites (EH3) are combined. The events outside of the GdLS volume are largely due to the accidental background events. The reconstruction still has large uncertainties and biases especially near the IAV edge [2]. Thanks to the design of the experiment, such uncertainties and biases do not enter the θ_{13} analysis.

Finally, the detected $\bar{\nu}_e$ candidates (background not subtracted) per day as a function of time is shown in Fig 11. Even though the reactor flux information is blinded, from the correlation of rate changes between ADs, one know the changes must be related to the reactor flux variation. In fact, core L2 has been off until Jan 8th, and core L1 has been off since Jan 20th (both cores are in Ling Ao, close to AD3).

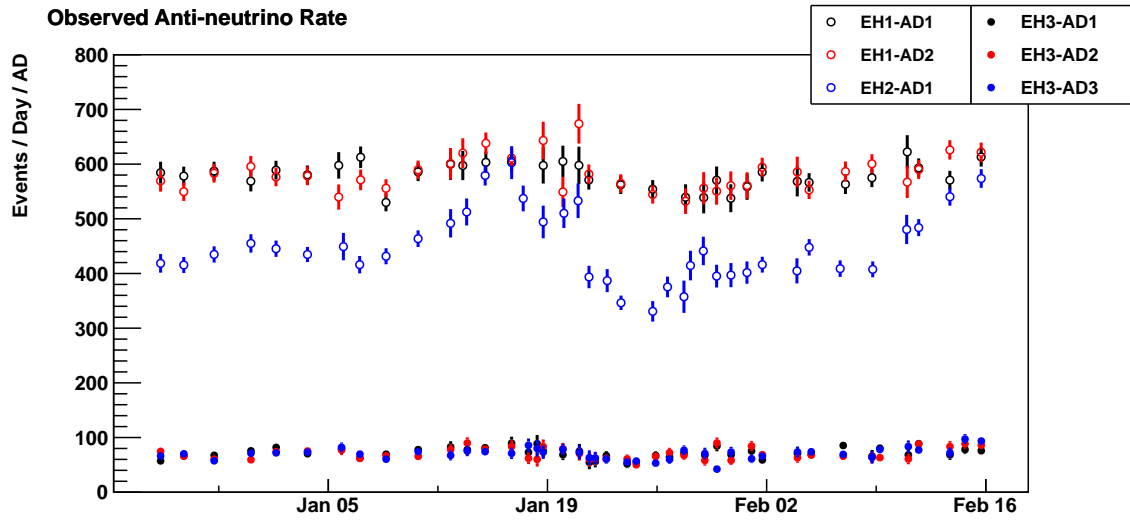


Figure 11. Detected $\bar{\nu}_e$ candidates per day as a function of time. Background is not subtracted from the candidates. Runs are combined such that each point has at least 8 hours.

2. Background Estimation

After applying the anti-neutrino selections discussed in section 1, the remaining background events can be divided into two categories:

- *Accidental Background*: Two uncorrelated events ‘accidentally’ passing the analysis cuts and mimic an IBD pair.
- *Correlated Background*: True correlated events that fake the IBD interaction. The possible correlated backgrounds are:
 - ${}^9\text{Li}/{}^8\text{He}$ from muon spallation
 - Fast neutrons from muon spallation
 - Correlated signals from ${}^{241}\text{Am}/{}^{13}\text{C}$ source
 - ${}^{13}\text{C}(\alpha, n){}^{16}\text{O}$ background

2.1 Accidental Coincidence

The accidental background is caused by a ‘prompt-positron-like’ single event ($0.7 \text{ MeV} < E_p < 12 \text{ MeV}$) and a ‘delayed-neutron-like’ single event ($6 \text{ MeV} < E_d < 12 \text{ MeV}$) randomly happen close in time ($\Delta T_{p-d} < 200 \mu\text{s}$) and fake an IBD pair. To estimate its rate, firstly we apply the same muon veto as in IBD selection (section 1.5) to remove the high event rate periods after muons:

- AD is vetoed $2 \mu\text{s}$ before any muons that are tagged by Water Pool or the same AD.
- AD is vetoed $200 \mu\text{s}$ after muons that are tagged by Water Pool.
- AD is vetoed 1 ms after muons that are tagged by the same AD.
- AD is vetoed 0.4 seconds after *Shower Muons* in the same AD.

Notice that here the additional veto of $200 \mu\text{s}$ before a muon and $400 \mu\text{s}$ after a muon from the DMC cut are not applied (they should only enter into the muon veto time calculation). Next, the same flasher cut as in IBD selection is applied to remove the flasher events. The remaining AD event spectra is shown in Fig. 12 (black lines), which are dominated by external radioactivities from the PMT and some contribution of external and internal radioactivities from liquids and other materials. The majority of those events are uncorrelated with each other, which we defined as (pure) *singles*. In contrast, a small fraction of events in Fig. 12 are *correlated* events, including the IBD paired events. For example, the peak around 8 MeV in the black line is mostly neutrons from the correlated IBD pairs. To obtain the pure singles, we then require that the adjacent events satisfy:

- no ‘prompt-like’ ($0.7 \text{ MeV} < E < 12 \text{ MeV}$) event within the previous $400 \mu\text{s}$
- no ‘delayed-like’ ($6 \text{ MeV} < E < 12 \text{ MeV}$) event within the following $200 \mu\text{s}$.

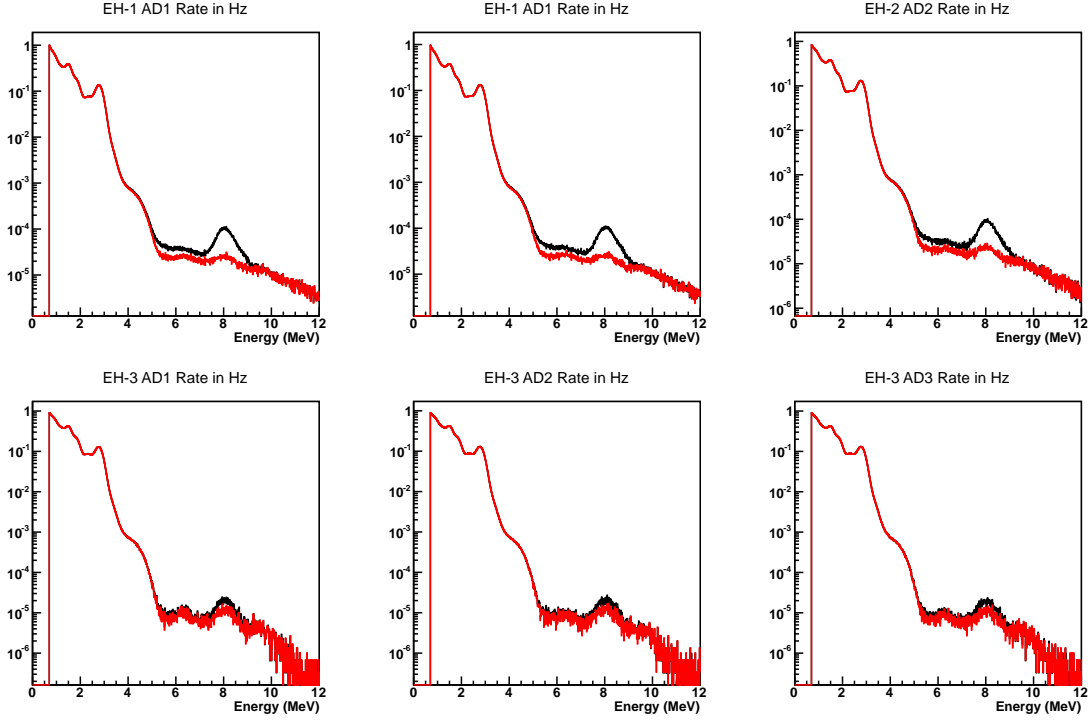


Figure 12. Singles spectra in all six ADs. Black line shows all triggers after muon veto and flasher cuts. Red line further removes temporal correlated triggers from the black line.

This requirement then removes the correlated events, predominated IBD pairs. The pure singles spectra is shown in Fig. 12 (red lines).

The pure ‘prompt-like’ ($0.7 \text{ MeV} < E < 12 \text{ MeV}$) singles rate and ‘delayed-like’ ($6 \text{ MeV} < E < 12 \text{ MeV}$) singles rate are defined as R_p and R_d respectively, and can be accurately calculated from the singles spectra on a run-by-run basis. By varying the veto range of coincidence time, we estimated a systematic uncertainty of 0.2% on calculating the singles rate. On average, R_p is on the order of $\sim 70 \text{ Hz}$ and R_d is on the order of a thousand events per day. The origin of the ‘delay-neutron-like’ singles is investigated in doc:7043 [16]. At near site, they are dominated by long-lived spallation beta-decay isotopes, such as ^{12}B . At far site, since muon rate is much smaller, the ‘delay-neutron-like’ singles are dominated by the neutrons from the $^{241}\text{Am}^{13}\text{C}$ sources parking on top of the AD, which capture on stainless steel and emit high energy gammas penetrating into the scintillator region. Evidence and simulation of the $^{241}\text{Am}^{13}\text{C}$ accidentals are shown in doc:7568 [18] and doc:6779 [17].

The rate R'_c that one ‘prompt-like’ and one ‘delayed-like’ singles happen within $(1\mu\text{s}, 200\mu\text{s})$ to fake an IBD pair can be calculated by

$$R'_c = P(1; R_p \cdot 199\mu\text{s}) \cdot R_d \quad (2.1)$$

where $P(k; \lambda) = \lambda^k e^{-\lambda} / k!$, is the Poisson probability of detecting k events while expecting λ events. The *decoupled multiplicity cut* (section 1.6) also requires

- No prompt candidate between $(200\mu\text{s}, 400\mu\text{s})$ before the delayed candidate

- No delayed candidate within $200\mu s$ after the delayed candidate

According to these DMC rules, the accidental background rate R_{acc} can now be calculated by

$$R_{acc} = P(0; R_p^a \cdot 200\mu s) \cdot P(0; R_d^a \cdot 200\mu s) \cdot R'_c \quad (2.2)$$

where R_p^a and R_d^a are the ‘all’ prompt-like and delayed-like event rate after muon veto and flasher cut, which equals the pure singles rate plus correlated event rate, such as IBD rate. In practice, $R_p^a \sim R_p$, and $P(0; R_d^a \cdot 200\mu s) \sim 1$, so the accidental rate becomes:

$$\begin{aligned} R_{acc} &= P(0; R_p \cdot 200\mu s) \cdot R'_c \\ &\sim (1 - R_p \cdot 200\mu s) \cdot R_p \cdot 199\mu s \cdot R_d \cdot (1 - R_p \cdot 200\mu s) \\ &\sim (1 - R_p \cdot 400\mu s) \cdot R_p \cdot 199\mu s \cdot R_d \end{aligned} \quad (2.3)$$

The accidental rate as a function of time in each AD is shown in Fig 13. The variation of the accidental rate is from the changes of R_p with time, which has a general trend of decreasing but sometimes jumps up. Reasons of the R_p variation are still under investigating. One possible cause is the correlation with Rn activities in the water.

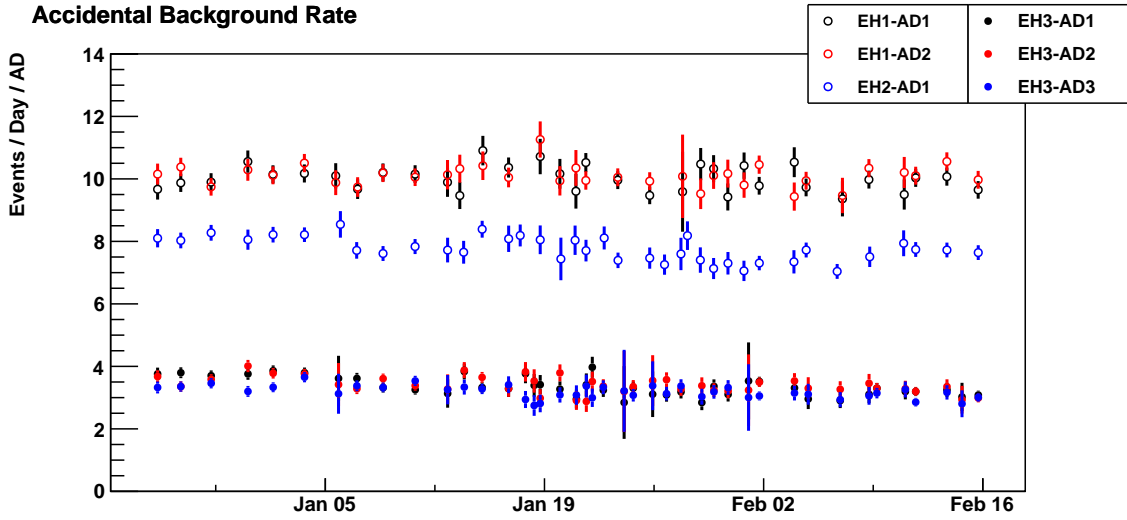


Figure 13. Accidental Rate as a Function of Time

Using the same data set as the anti-neutrino selection, the total expected accidental background in each AD is summarized in table 6. The reported rate is before the muon veto and multiplicity cut efficiency correction.

A less precise but independent estimation of the accidental background can be made directly from the anti-neutrino candidates. Unlike the true IBD pairs, the temporal correlated accidental pairs have no spacial correlation. The distribution of distance between the prompt and the delayed event for IBD candidates is shown in Fig 9(d). A cut at $\Delta r > 1.8m$ selects 1.2% of the candidates at near sites and 3.6% at far sites, which are mostly from accidentals. From toy MC, it will select $\sim 75\%$ of all accidentals. The numbers agree with the estimations from singles. Since we can

Table 6. Summary of Accidental Background

	Daya Bay		Ling Ao	Far		
	AD1	AD2	AD1	AD1	AD2	AD3
Rate [/day/AD]	10.00	10.11	7.76	3.37	3.43	3.21
Uncertainty [/day/AD]	0.06	0.06	0.05	0.03	0.03	0.03
% in IBD Candidates	1.4%	1.4%	1.4%	4.5%	4.6%	4.3%

accurately calculate the accidental background rate, spacial correlation cut is not required in the IBD selections, in order to avoid the vertex reconstruction uncertainties.

(More details on the accidental background study are documented in doc:7679 [15].)

2.2 ${}^9\text{Li}/{}^8\text{He}$

As discussed in section 1.5, the long lived spallation ${}^9\text{Li}$ ($\tau_{1/2} = 178.3\text{ ms}$, $Q = 13.6\text{ MeV}$) and ${}^8\text{He}$ ($\tau_{1/2} = 118.5\text{ ms}$, $Q = 10.7\text{ MeV}$) can give correlated beta-neutron signals and fake the IBD events. The shower muon veto

- AD is vetoed 0.4 seconds after *Shower Muons* ($\text{PE} > 3 \times 10^5$) in the same AD.

is designed to remove most of the ${}^9\text{Li}/{}^8\text{He}$ background. From previous underground experiments such as KamLAND, the ${}^9\text{Li}$ production is much higher than ${}^8\text{He}$. Given the half-life, this veto removes 80% of the spallation ${}^9\text{Li}$ that are from shower muons. The shower muon veto reduces the analysis live time by about 5% at near sites, but only about 0.6% at the far site.

To estimate the absolute number of the ${}^9\text{Li}/{}^8\text{He}$ background, we invert the shower muon cut to select the anti-neutrino candidates close to the shower muons. In other words, we require triple coincidence to identify a ${}^9\text{Li}/{}^8\text{He}$ event: shower muon + prompt-beta-like + delayed-neutron-like signals. We also vary the light yield of the shower muon definition, to study the efficiency of selecting the ${}^9\text{Li}/{}^8\text{He}$ events. The distribution of event time to the previous ‘shower muon’ is fitted with the formula (doc:7278 [19]):

$$f(t) = \sum_i N_i \cdot (\lambda_\mu + \lambda_i) e^{-(\lambda_\mu + \lambda_i)t} + N_r \cdot \lambda_\mu e^{-\lambda_\mu t} \quad (2.4)$$

Where λ_μ is the ‘muon’ (after analysis cuts) rate in study. N_i is the number of spallation isotope i produced by the muons and λ_i is the decay time of the isotope i . The last term represents the contribution from random events that have no correlation with the muons, such as true anti-neutrinos. The last term follows the expected exponential distribution from the ‘muon’ rate. When the ‘muon’ rate is much lower than the isotope decay rate, the distribution simplifies to:

$$f(t) = \sum_i N_i \cdot \lambda_i e^{-\lambda_i t} + N_r \cdot \lambda_\mu e^{-\lambda_\mu t} \quad (2.5)$$

On the other hand, when the muon rate is much higher than the isotope decay rate, it becomes difficult to fit the isotope contribution from the distribution.

An example of the fit for EH1 candidates generated by the shower muon ($\text{PE} > 3 \times 10^5$, $\sim E_\mu > 1.75\text{ GeV}$) are shown in Fig. 14 In this fit, events with $\Delta r > 1.2m$ are removed, which are

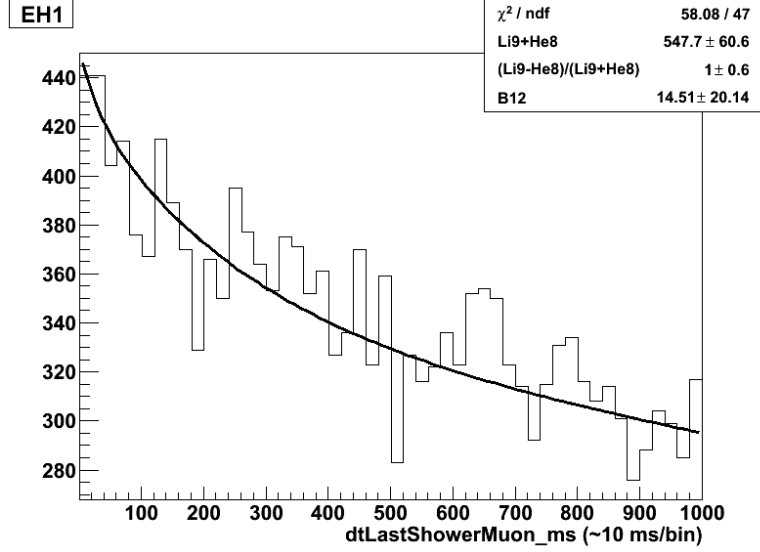


Figure 14. Distribution of time between ${}^9\text{Li}/{}^8\text{He}$ candidates and the previous shower muon

mostly accidental coincidence whose delayed-like signal comes from long lived isotopes such as ${}^{12}\text{B}/{}^{12}\text{N}$ and ${}^8\text{Li}/{}^8\text{B}$, since those events have actual correlation with muons and may bias the fit. The result of the fit is summarized in Table 7.

Table 7. Summary of number of ${}^9\text{Li}/{}^8\text{He}$ from shower muons

	Daya Bay	Ling Ao	Far
$E_\mu > 1.75 \text{ GeV}$ [events]	680 ± 190	232 ± 70	51 ± 14

There may still be ${}^9\text{Li}/{}^8\text{He}$ that are not generated by shower muons. They will escape the shower muon veto and mimic the IBD candidate. To investigate, we further divide the muon sample into the following categories:

- *n-shower muons*: muons with Gd capture neutrons in the $(20\mu\text{s}, 200\mu\text{s})$ window following the muon.
- *non-n-shower muons*: muons that do not have Gd capture neutrons in the $(20\mu\text{s}, 200\mu\text{s})$ window following the muon.

We fit the the time to muon distribution and estimated the number of ${}^9\text{Li}/{}^8\text{He}$ in each muon category. The result of *non-n-shower muons* is consistent with zero. The result of *n-shower muons* in different muon energy range is summarized in Table 8. As can be seen, in the Daya Bay site, there are about 30% of the ${}^9\text{Li}/{}^8\text{He}$ produced by low energy shower muons. In Ling Ao and Far site, ${}^9\text{Li}/{}^8\text{He}$ production is dominated by higher energy shower muons. The inefficiency of only selecting *n-shower muons* can be estimated by compare the first row of the table, and the result from the fit of all shower muons (Table 7). The total expected ${}^9\text{Li}/{}^8\text{He}$ production at each experimental hall is summarized in Table 9 The estimated rate at each site is consistent with the $E_\mu^{0.73}$ power law.

Table 8. Summary of number ${}^9\text{Li}/{}^8\text{He}$ from n-shower muons

	Daya Bay	Ling Ao	Far
$E_\mu > 1.75 \text{ GeV}$ [events]	620 ± 60	143 ± 25	36 ± 7
$0.5 \text{ GeV} < E_\mu < 1.75 \text{ GeV}$ [events]	210 ± 60	18 ± 29	1 ± 4
$E_\mu < 0.5 \text{ GeV}$ [23] [events]	110 ± 40	6 ± 14	5 ± 2

Table 9. Summary of ${}^9\text{Li}/{}^8\text{He}$ production rate at each site

	Daya Bay	Ling Ao	Far
${}^9\text{Li}/{}^8\text{He}$ production rate [day/AD]	5.79 ± 1.23	4.61 ± 1.49	0.55 ± 0.14

Using the same data set as used in the anti-neutrino selection, after applying the shower muon veto, the remaining ${}^9\text{Li}/{}^8\text{He}$ background is summarized in table 10. The ${}^9\text{Li}/{}^8\text{He}$ background is expected to be the same for ADs in the same experimental hall, since it's correlated with the muon flux and energy spectra at the site. The reported rate is before the muon veto and multiplicity cut efficiency correction.

Table 10. Summary of remaining ${}^9\text{Li}/{}^8\text{He}$ background at each experimental hall

	Daya Bay	Ling Ao	Far
Rate [day/AD]	2.74 ± 0.64	1.45 ± 0.89	0.16 ± 0.08
% in IBD Candidates	0.38%	0.27%	0.20%

(More details on the ${}^9\text{Li}/{}^8\text{He}$ background study are documented in doc:7653 [22].)

2.3 Fast Neutrons

As discussed in section 1.5, fast neutrons produced by muons could enter the AD and give coincidence events that mimic the $\bar{\nu}_e$ events. If the parent muon is not detected by water pool or the AD, either from inefficiency of the veto system, or from muons outside of the veto system, the fast neutron will escape the muon veto cut and contribute to the IBD background.

We use three methods to study the remaining fast neutron background

- Look for high energy IBD candidates above 8.5 MeV, where the reactor neutrino spectra drop to negligible level and most contributions are from fast neutrons.
- Look for IBD candidates in coincidence with the WP muons, which are mostly from fast neutrons.
- Look for IBD candidates in coincidence only with RPC muons, which are mostly from fast neutrons from muons that don't pass the water veto system (but pass the RPC).

In the first method, when looking for high energy IBD candidates, we need to raise the energy threshold definition of *AD muon*, since otherwise the high energy fast neutrons will be considered as an *AD muon*. In the second method, we need to require the prompt signal to be in coincidence with Inner WP within 300 ns, to select only the prompt neutron recoil signals. We further require

the multiplicity (the number of prompt-delayed pairs that can be formed after a muon) equals 1, to select clean sample of fast neutrons. The delayed signal is also required to be $12 \mu\text{s}$ away from the muon, to remove the Michel electron contribution. In the third method, we look for high energy IBD candidates after the muon veto, but is in coincidence with RPC 3/4 triggers. These presumably come from the fast neutrons that are generated by muons only pass through the RPC system [25].

The prompt energy spectrum of fast neutron tagged by each method is shown in Fig. 15.

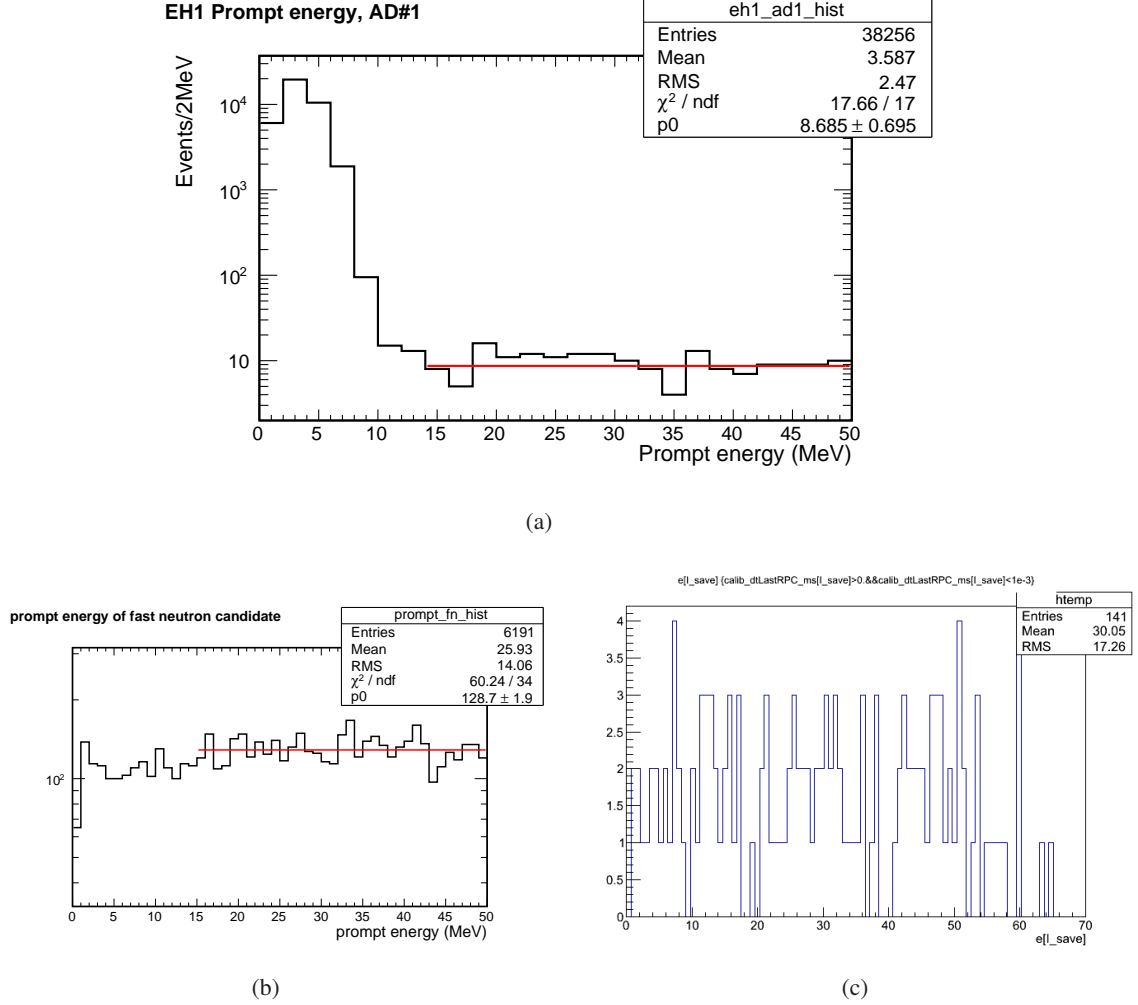


Figure 15. Prompt energy spectrum of fast neutron tagged by (a) AD; (b) Water Pool; (c)RPC.

All three methods suggest a flat prompt energy spectrum within 30% systematic uncertainty. Assuming this, we use the the high energy IBD candidates to extrapolate to the energy range (0.7MeV, 12MeV) to predict the expected remaining fast neutrons background. The fast neutron background is expected to be the same for ADs in the same experimental hall, since it's correlated with the muon flux and energy spectra at the site. The total expected fast neutron background at each experimental hall in the same data set as used in the anti-neutrino selection, is summarized in table 11. The reported rate is before the muon veto and multiplicity cut efficiency correction.

(More details on the fast neutron background study are documented in doc:7539 [24].)

Table 11. Summary of fast neutron background at each experimental hall

	Daya Bay	Ling Ao	Far
Rate [/day/AD]	0.95 ± 0.28	0.71 ± 0.22	0.07 ± 0.02
% in IBD Candidates	0.13%	0.13%	0.09%

2.4 Correlated $^{241}\text{Am}^{13}\text{C}$ Background

The $^{241}\text{Am}^{13}\text{C}$ sources (0.5 Hz neutron rate) parking on top of the ADs can cause correlated background. It is mainly caused by two correlated high energy gammas from one $^{241}\text{Am}^{13}\text{C}$ neutron. The prompt signal comes from neutron inelastic scattering on stainless steel, and the delayed signal comes from the neutron capture on stainless steel. The two gammas have a small probability of entering the AD together causing correlated events.

A simulation has been performed (doc:6779 [17]) to study this background. By taking the yield ratio of correlated over uncorrelated AmC background from simulation, and the measured rate of uncorrelated AmC background from data (doc:7568 [18]), we estimated the correlated $^{241}\text{Am}^{13}\text{C}$ background rate to be 0.2 ± 0.2 events/day/AD for all ADs. The 100% relative uncertainty on the background is conservatively estimated from the simulation [17].

2.5 $^{13}\text{C}(\alpha, n)^{16}\text{O}$ Background

Radioactive impurities in GdLS, during their decay chains, emit α particles. The visible energies of these α particles are heavily quenched down to below 1 MeV, however, the second order (α, n) reactions could produce energetic neutrons. The thermalization and capture of those fast neutrons then give prompt-delayed signals and mimic the $\bar{\nu}_e$ events. More than 90% of the α activity in GdLS comes from the decay of ^{210}Po (doc:7509 [20]), who is the daughter nucleus of ^{210}Pb and was introduced by means of ^{222}Rn contamination possibly from the initial handling of acrylic vessel.

^{210}Po has a half life of 138 days and emits an α particle with kinetic energy of 5.304 MeV. In natural carbon, 1.1% is ^{13}C . The $^{13}\text{C}(\alpha, n)^{16}\text{O}$ reaction has a Q value of 2.22 MeV (zero threshold). At α particle energy 5.304 MeV, the final state of ^{16}O can be its ground state, first excited state or second excited state. The prompt signal from $^{13}\text{C}(\alpha, n)^{16}\text{O}$ background thus consists of the following events:

- The neutrons from the $^{13}\text{C}(\alpha, n)^{16}\text{O}^{\text{g.s.}}$ reaction typically have energies from 3 MeV to 7 MeV. Most of them lose energy by elastically scattering on ^1H nuclei during thermalization, and the recoiled protons could give visible energies above the analysis threshold of 0.7 MeV. The neutrons from reactions involving ^{16}O 1st or 2nd excited state typically have energies below 1 MeV contribute little to the prompt signal.
- High energy neutrons sometimes inelastically scatter on ^{12}C and excite the nucleus to its first excited state. The $^{12}\text{C}^*$ then emits a 4.438 MeV γ particle during de-excitation.
- If the final state of ^{16}O is its 1st excited state, the $^{16}\text{O}^*$ returns to its ground state by emitting an e^+e^- pair with total energy of 6.049 MeV.

- If the final state of ^{16}O is its second excited state, the $^{16}\text{O}^*$ returns to its ground state by emitting a 6.129 MeV γ ray.

From the measured alpha rate combined with the $^{13}\text{C}(\alpha, n)^{16}\text{O}$ cross sections, the (α, n) background is estimated in doc:7509 [20] to be 0.007% in AD1/2/3 and 0.05% in AD 4/5/6 compared to the IBD rate, much smaller compared with other backgrounds. The rate in each AD is summarized in table 12

Table 12. Summary of $^{13}\text{C}(\alpha, n)^{16}\text{O}$ background

	Daya Bay		Ling Ao	Far		
	AD1	AD2	AD1	AD1	AD2	AD3
Rate [/day/AD]	0.04 ± 0.02	0.04 ± 0.02	0.035 ± 0.02	0.03 ± 0.02	0.03 ± 0.02	0.03 ± 0.02

2.6 Summary of Background Estimation

Table. 13 summarizes all expected backgrounds in the data set. The total number of background events is dominated by the accidentals, but the uncertainty on the backgrounds is dominated by $^9\text{Li}/^8\text{He}8$, fast neutron and correlated $^{241}\text{Am}^{13}\text{C}$ backgrounds.

Table 13. Summary of observed signals and estimated backgrounds [events]

	Daya Bay		Ling Ao	Far		
	AD1	AD2	AD1	AD1	AD2	AD3
DAQ live time [days]	49.5527	49.5527	49.4968	48.9453	48.9453	48.9453
$\bar{\nu}_e$ candidate [events]	28692	28857	22169	3536	3464	3461
Accidentals [events]	393.6	396.4	317.4	157.7	160.3	150.1
$^9\text{Li}/^8\text{He}8$ [events]	107.9	107.4	59.3	7.5	7.5	7.5
Fast Neutron [events]	37.4	37.2	29.0	3.3	3.3	3.3
Correlated $^{241}\text{Am}^{13}\text{C}$ [events]	7.9	7.8	8.2	9.4	9.4	9.4
$^{13}\text{C}(\alpha, n)^{16}\text{O}$ [events]	1.6	1.6	1.4	1.4	1.4	1.4
Total Expected B.G. [events]	548.3	550.5	415.4	179.2	181.8	171.6
B.G. Uncertainty [events]	28.3	28.2	38.2	10.3	10.2	10.2

3. Signal Estimation

3.1 Target Protons

The target volume for IBD interaction is the GdLS volume inside the 3-meter inner acrylic vessel (IAV), up to the top of its conical lid. The mass of the filled GdLS is blinded, but it should be very close to the nominal designed value of 20 tons. The amount of GdLS in the central overflow tank is precise monitored by sensors, and should be subtracted from the filled GdLS mass after unblinding. There is also 3.7kg in the pipes connecting the Gd-LS in IAV and the overflow tank that should be subtracted from the filled mass.

Chemical combustion method is used (doc:6615 [21]) to measure the hydrogen mass fraction based on the amount of water obtained after ‘burning’ Gd-LS. The central value of 11.99%(1 ± 0.42%) is used as the nominal value. The uncertainty is correlated between ADs, since it’s determined by the same method.

The total number of target protons can be calculated by

$$N_p = N_A \cdot m_{\text{target}} \cdot f_H / m_H \cdot I_{1H} \quad (3.1)$$

where $N_A = 6.02214 \times 10^{23}$ is the Avogadro number, m_{target} is the (blinded) target mass, $f_H = 0.1199$ is the hydrogen mass fraction, $m_H = 1.007825 \text{ g/cm}^3$ is the hydrogen atomic mass and $I_{1H} = 0.99985$ is the isotopic abundance of ^1H and . By taking the nominal values, the total number of target protons becomes:

$$N_p = 1.4327 \times 10^{30} \cdot (m_{\text{target}}/20 \text{ ton}) \quad (3.2)$$

After unblinding, the time-averaged target mass of each AD during the data period is listed in Table 14 (doc:7714). The overall mass variation due to the temperature change is less than 3 kg.

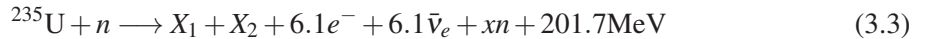
Table 14. Time-averaged target mass of each AD [ton].

Daya Bay		Ling Ao	Far		
AD1	AD2	AD1	AD1	AD2	AD3
19.941	19.966	19.891	19.913	19.991	19.892

3.2 Reactor Anti-neutrino Flux

The vast majority of $\bar{\nu}_e$ ’s detected in Daya Bay come from six nuclear reactors nearby, two at Daya Bay and four at Ling Ao. Besides providing $\bar{\nu}_e$ ’s for scientists, these nuclear power plants distributes large amount of electric power to the general public. The true baselines between ADs and reactors are unblinded and listed in Table 15. The uncertainty of the flux due to the precision of the baseline survey (28 mm) is less than 0.01%.

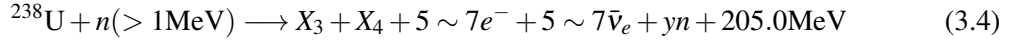
Four main fissile nuclei ^{235}U , ^{238}U , ^{239}Pu and ^{241}Pu contribute to 99.9% of the $\bar{\nu}_e$ ’s from the nuclear reactors. ^{235}U is the initial fuel enriched to $\sim 3\text{--}4\%$ of the uranium. It fissions with thermal neutrons as follows:



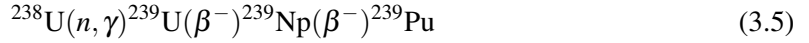
	D1	D2	L1	L2	L3	L4
AD1	362.377	371.759	903.471	817.162	1353.62	1265.32
AD2	357.937	368.411	903.351	816.9	1354.23	1265.89
AD3	1332.47	1358.14	467.571	489.574	557.58	499.207
AD4	1919.63	1894.34	1533.18	1533.62	1551.38	1524.94
AD5	1917.52	1891.97	1534.92	1535.03	1554.76	1528.04
AD6	1925.25	1899.86	1538.93	1539.47	1556.34	1530.08

Table 15. Baseline [m] between ADs and reactor cores. The six reactor cores are grouped into three reactor complex: Daya Bay (D1, D2), Ling Ao I (L1, L2), Ling Ao II (L3, L4).

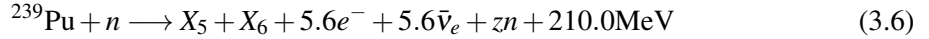
where X_1 and X_2 are the daughter fission fragment nuclei such as ^{94}Zn and ^{140}Ce . ^{238}U , on the other hand, can only fission with fast neutrons:



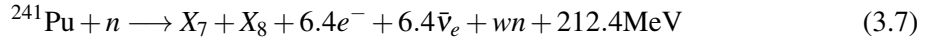
^{238}U can also capture a neutron and through subsequent β decays breeds another fissionable isotope ^{239}Pu :



^{239}Pu fissions with thermal neutrons as follows:



Or it could sequentially capture two neutrons and produce another fissionable isotope ^{241}Pu , which then fissions with thermal neutron as follows:



On average, 6 $\bar{\nu}_e$'s and 200 MeV energy are released in each fission, however, only about 1.8 $\bar{\nu}_e$'s are above the 1.8 MeV IBD interaction threshold. A typical 3 GWth reactor produces $\sim 5 \times 10^{20}$ $\bar{\nu}_e$'s per second.

During one fuel cycle, the fission isotope fraction changes with time. Basically, ^{235}U is depleted and ^{239}Pu is bred, a process called 'burn-up'. To accurately calculate the reactor neutrino flux, the instantaneous fission fraction and thermal power are needed. This information comes from the power plant company, and is blinded. Once unblinded, it will be delivered to general collaborators on a weekly averaged basis. In the blind analysis, we adopt 2.895 GW as the nominal reactor thermal power, and $^{235}\text{U} : ^{238}\text{U} : ^{239}\text{Pu} : ^{241}\text{Pu} = 0.64 : 0.08 : 0.25 : 0.03$ as the relative fission fraction.

Following the method outlined in [28], the instantaneous anti-neutrino flux $S(E_\nu)$ for a reactor core is estimated as,

$$S(E_\nu) = \frac{W_{th}}{\sum_i (f_i/F) e_i} \sum_i^{\text{isotopes}} \left(\frac{f_i}{F} \right) s_i(E_\nu). \quad (3.8)$$

where W_{th} is the thermal power of the reactor core, $\bar{f}_i = f_i/F$ is the relative fission rate of each isotope, e_i is the average energy released by a single fission of each isotope and $s_i(E_\nu)$ is the

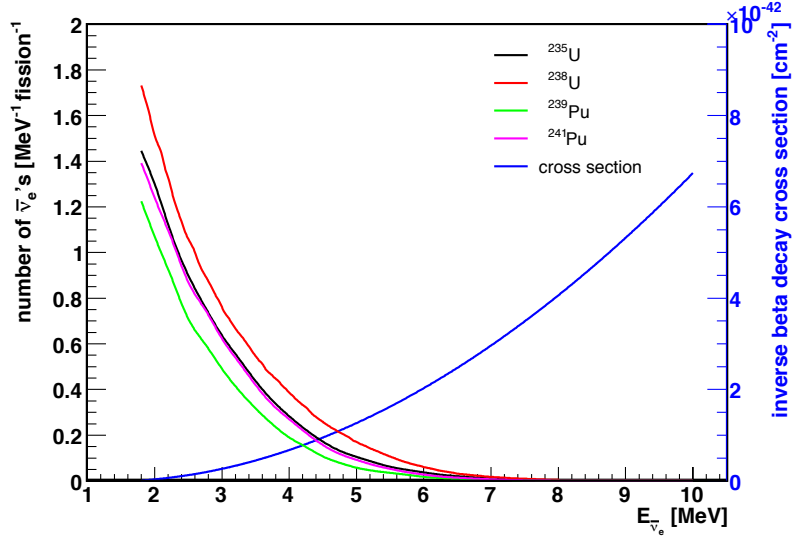


Figure 16. The $\bar{\nu}_e$ energy spectrum from different fission isotope ^{235}U , ^{238}U , ^{239}Pu and ^{241}Pu . The inverse beta decay cross section as a function of $\bar{\nu}_e$ is show in blue line.

average antineutrino energy spectrum due to a single fission of each isotope. $s_i(E_\nu)$ is shown in Fig. 16. The $\bar{\nu}_e$ energy spectra from fissions of ^{235}U , ^{239}Pu , ^{241}Pu are deduced from the measured beta spectra at ILL high flux reactor in Grenoble [29, 30]. The $\bar{\nu}_e$ spectrum from fission of ^{238}U is calculated theoretically [31], since ^{238}U only fissions with fast neutrons and lacks experimental data. The uncertainty of the total $\bar{\nu}_e$ spectrum shape is estimated from the rate-weighted sum of the uncertainty of each spectrum of the isotope [29, 30, 31] to be 2.5%.

The spectrum of antineutrinos detected by detector j due to reactor core k is estimated as,

$$S_{jk}(E_\nu) = T_j \varepsilon_j \sigma(E_\nu) \frac{P_{ee}(E_\nu, L_{jk})}{4\pi L_{jk}^2} S_k(E_\nu). \quad (3.9)$$

The number of protons in the target region of each detector is T_j , and the efficiency of each detector is ε_j . The cross-section for inverse beta decay is $\sigma(E_\nu)$. The $\bar{\nu}_e$ to $\bar{\nu}_e$ oscillation probability P_{ee} depends on the antineutrino energy E_ν and the reactor to detector distance L_{jk} .

$$P_{ee} = 1 - \sin^2 2\theta_{13} \sin^2 \Delta_{31} - \cos^4 \theta_{13} \sin^2 2\theta_{12} \sin^2 \Delta_{21} \quad (3.10)$$

where

$$\Delta_{ij} = \sin^2 \left(1.267 \frac{\Delta m_{ij}^2 [\text{eV}^2] \cdot L [\text{m}]}{E [\text{MeV}]} \right) \quad (3.11)$$

In Eqn. 3.10, the approximation $\Delta m_{31}^2 = \Delta m_{32}^2$ is assumed. The third term in Eqn. 3.10 is the contribution from solar mixing angle and mass difference. At $\sin^2 2\theta_{13} = 0.1, L = 2\text{km}$, the third term is only about 3% relative to the second term.

The cross section of inverse beta decay is given in Ref. [32] and is shown as a function of $\bar{\nu}_e$ energy in Fig. 16. The cross section can be expressed, neglecting terms of order of E_ν/M , in terms

of the neutron lifetime and the phase-space factor $f_{p.s.}^R = 1.7152$ [33] as

$$\sigma_{\text{tot}}^{(0)} = \frac{2\pi^2/m_e^5 E_e^{(0)} p_e^{(0)}}{f_{p.s.}^R \tau_n} \quad (3.12)$$

In this way, the cross section is tied directly to the neutron lifetime. The small (order E_ν/M) energy-dependent outer radiative corrections to σ_{tot} [34] are not negligible and are included in the calculation shown in Fig. 16. The total systematic uncertainty from the inverse beta decay cross section is estimated to be 0.2%.

The detection rate R_{jk} can be obtained by integrating over antineutrino energy,

$$R_{jk} = \frac{T_j \epsilon_j}{4\pi L_{jk}^2} \int P_{ee}(E_\nu, L_{jk}) \sigma(E_\nu) S_k(E_\nu) dE_\nu. \quad (3.13)$$

For convenience, the un-oscillated integrated spectrum is defined as $\bar{F} = \int \sigma(E_\nu) S_k(E_\nu) dE_\nu$, and the average oscillation probability is given as \bar{P}_{ee} . The rate can then be expressed more compactly as,

$$R_{jk} = T_j \epsilon_j \bar{F}_k \frac{\bar{P}_{ee,jk}}{4\pi L_{jk}^2}. \quad (3.14)$$

The number of protons, T_j , and the detector efficiency, ϵ_j depend only on the given detector. The mean reactor flux, \bar{F}_k , depends only on the reactor core. The remaining terms depend on the distance between the detector and reactor. The average oscillation survival probability, $\bar{P}_{ee,jk}$, is determined by the values of the neutrino oscillation parameters chosen by nature, and has only minor dependence on the differences in the antineutrino energy distributions between reactors.

The total number of inverse beta decay events for a detector, N_j , is the integral of the reactor anti-neutrino interaction rate R_{jk} over the time periods that the detector is live,

$$N_j = \sum_k^{\text{cores}} \int R_{jk} dt_{\text{live}}. \quad (3.15)$$

We obtain the reactor information as a livetime-weighted average over a one week period, \bar{R}_{jk} . For this case, the integral is converted to a sum over the weekly live time, Δt_l ,

$$N_j = \sum_k^{\text{cores}} \sum_l^{\text{week}} \bar{R}_{jk} \Delta t_l. \quad (3.16)$$

3.3 Summary of Signal Estimation

By assuming all nominal values as discussed above, and all 6 reactor cores on, we calculated the expected total number of IBD interactions per day inside the target (GdLS) volume. The result is listed in the first row of Table. 16. After applying all analysis cuts as discussed in section 1, the expected number of detected $\bar{\nu}_e$ events is listed in the second row of Table. 16.

Assuming $\sin^2 2\theta_{13} = 0.1$, as hinted by previous experiments such as Double Chooz and T2K, we calculated the weighted average survival probability $\bar{P}_{ee,j}$ at each detector when all six reactor cores are at the same nominal power and on the same fission curve. The result is listed in Table 17.

Table 16. Expected IBD events/day at each detector

	Daya Bay		Ling Ao	Far		
	AD1	AD2	AD1	AD1	AD2	AD3
IBD interaction rate [/day]	987.8	1004.8	900.1	118.3	118.2	117.6
After analysis cuts [/day]	629.8	638.0	597.0	90.9	90.5	90.1

Table 17. Weighted average survival probability at each detector, assuming $\sin^2 2\theta_{13} = 0.1$ and all six reactor cores are at the same nominal power and on the same fission curve.

	Daya Bay		Ling Ao	Far		
	AD1	AD2	AD1	AD1	AD2	AD3
Survival Probability	0.982	0.982	0.980	0.920	0.920	0.920

The total systematic uncertainties on the signal prediction is listed in Table. 18. The systematics are broken into three categories. The ‘AD Correlated Uncertainty’ is the uncertainty that affects all detectors in the same magnitude. In other words, it is the absolute normalization of the rate prediction. θ_{13} measurement is not sensitive to this absolute uncertainty. The ‘AD Uncorrelated Uncertainty’ indicates the size of relative AD-to-AD variation. They are directly related to the sensitivity of θ_{13} measurement. The ‘Reactor Uncorrelated Uncertainty’ indicates the size of relative core-to-core flux variation. The variation affects all detectors but with different magnitude weighted by the baseline. The implied weakened detector correlations makes θ_{13} measurement only marginally sensitive to the core-to-core variation.

Table 18. Summary of Systematic Uncertainties on IBD Rate Prediction

	AD Correlated	AD Uncorrelated	Reactor Uncorrelated
Reactor Power/Fission	2.0%		2.0%
Spent fuel			0.3%
Neutrino Spectra	2.5%		
IBD Cross Section	0.5%		
Target Protons	0.5%	0.02%	
Efficiency of Cuts	0.9%	0.28%	
Total Systematic Uncertainty	3.4%	0.28%	2.0%

3.4 Absolute Flux Measurement

With the unblinded period from 22 Sept, 2011 to 23 Dec, 2011, an absolute measurement of reactor $\bar{\nu}_e$ flux can be made with AD1 and AD2. Even though with the relative measurement of near and far detectors, the θ_{13} analysis is not sensitive to the absolute flux, still this is a consistency check of our understanding of the reactor fluxes, and opens possibility of sterile neutrino searches.

The details of AD 1/2 periods result is summarized in Table 19. The ratio of observed $\bar{\nu}_e$ events (background subtracted) over expected $\bar{\nu}_e$ events assuming no oscillation is:

$$R_{AD1} = 0.986 \pm 0.006(stat.) \pm 0.034(syst.)$$

$$R_{AD2} = 0.982 \pm 0.006(stat.) \pm 0.034(syst.) \quad (3.17)$$

The ratio is consistent with 1 within the systematic uncertainty. In other words, due to the large uncertainty on the reactor flux, near site has no sensitivity on the θ_{13} . It might be a coincidence that the deficit is actually consistent with $\sin^2(2\theta_{13}) = 0.1$.

Table 19. Results from unblinded AD 1/2 period.

	AD1	AD2
Common AD Efficiency	0.8026	
Muon Veto Cut Efficiency	0.8129	0.8090
Multiplicity Cut Efficiency	0.9749	0.9752
Daq Live Time [days]	70.14	70.14
Observed $\bar{\nu}_e$ Candidate [events]	32589	32886
Total Expected Background [events]	787.6	788.0
Background Subtracted Observed $\bar{\nu}_e$ Events	31801.4	32098.0
Expected $\bar{\nu}_e$ Events	32252.4	32667.0
Observed / Expected	0.986	0.982

4. Theta13 Analysis and Results

4.1 Rate-only χ^2 Model Definition

A simple approach to estimate θ_{13} relies only on the measured number of events in each detector. This *rate-only* method is equivalent to fitting a histogram where the number of bins is equal to the number of detectors in the study. There are well-developed standard techniques for fitting histograms. Following Eq. [33.12] from [35], the χ^2 constructed from the Poisson likelihood comparing a measured number of entries N^{obs} with an expected value N^{exp} is,

$$\chi^2(\boldsymbol{\theta}) = -2\ln\lambda(\boldsymbol{\theta}) = 2 \left(N^{exp}(\boldsymbol{\theta}) - N^{obs} + N^{obs} \ln \frac{N^{obs}}{N^{exp}(\boldsymbol{\theta})} \right), \quad (4.1)$$

The expected value N^{exp} is predicted by a model with the parameters $\boldsymbol{\theta}$, including the expected background, while the observed number N^{obs} is measured from the data.

A common approach to account for model uncertainty is to include penalty terms δ_m , each constrained by the corresponding uncertainty, σ_m . For the specific case of the expected rate of antineutrino interactions in detector j due to reactor core k , we can replace the nominal rate R_{jk} with a modified rate \tilde{R}_{jk} ,

$$\tilde{R}_{jk} = R_{jk}(1 + \delta^{corr})(1 + \delta_j^{AD})(1 + \delta_k^r). \quad (4.2)$$

The systematic uncertainty terms has been discussed in section 3 and summarized in Table. 18. Any uncertainties that are correlated across all detectors or reactors are combined in σ^{corr} . All uncertainties which are specific to one detector or one reactor are combined into σ_j^{AD} or σ_k^r respectively.

In a similar fashion, the estimate of expected backgrounds b_{jn} can be replaced with \tilde{b}_{jn} ,

$$\tilde{b}_{jn} = b_{jn}(1 + \delta_{jn}^b). \quad (4.3)$$

where n enumerates over each background type that is discussed in section 2: accidentals, ${}^9\text{Li}/{}^8\text{He}$, fast neutrons, correlated ${}^{241}\text{Am}/{}^{13}\text{C}$ and ${}^{13}\text{C}(\alpha, n){}^{16}\text{O}$. The background uncertainties σ_{jn}^b is actually not all independent, for example, ${}^9\text{Li}/{}^8\text{He}$ and fast neutrons are correlated at the same site, and ${}^{241}\text{Am}/{}^{13}\text{C}$ uncertainties are correlated in all ADs. In practice, it is useful to remove degeneracy between penalty parameters. In rate analysis, all background terms are summed and is dominated by the accidentals. The other backgrounds are less than 0.6% compared with IBD signals so the precise treatment of uncertainty is not necessary. In the following presented analysis, all background terms in each AD are combined into one

$$\tilde{b}_j = b_j(1 + \delta_j^b). \quad (4.4)$$

and δ_j^b is assumed to be un-correlated among ADs. The expected number of events in detector j then becomes

$$N_j^{exp} = \tilde{N}_j + \tilde{B}_j = \sum_{\Delta T}^{weeks} \left(\sum_k^{cores} \tilde{R}_{jk} + \tilde{b}_j \right). \quad (4.5)$$

The distortion from penalty terms are included in the expected number of reactor antineutrino and background events, \tilde{N}_j and \tilde{B}_j respectively.

The total χ^2 including all detectors and penalty terms is,

$$\chi^2(\boldsymbol{\theta}) = 2 \sum_j^{ADs} \left(N_j^{exp}(\boldsymbol{\theta}) - N_j^{obs} + N_j^{obs} \ln \frac{N_j^{obs}}{N_j^{exp}(\boldsymbol{\theta})} \right) + \chi_{penalty}^2 \quad (4.6)$$

where the penalty component is,

$$\chi_{penalty}^2 = \left(\frac{\delta^{corr}}{\sigma^{corr}} \right)^2 + \sum_j^{ADs} \left(\frac{\delta_j^{AD}}{\sigma_j^{AD}} \right)^2 + \sum_k^{cores} \left(\frac{\delta_k^r}{\sigma_k^r} \right)^2 + \sum_j^{ADs} \left(\frac{\delta_j^b}{\sigma_j^b} \right)^2 + \sum_m^{osc} \left(\frac{\delta_m^{osc}}{\sigma_m^{osc}} \right)^2. \quad (4.7)$$

Each penalty parameter δ contributes to the χ^2 according to the independently measured uncertainty σ . Deviations of neutrino oscillation parameters from existing measurements, δ_m^{osc} , may be included as shown in the final term. This term assumes a Gaussian character for the uncertainties from existing oscillation parameter measurements. An external χ_{osc}^2 constrained by data from existing experiments is more rigorous, but is not used in this primitive study.

If we remove δ^{corr} from the χ^2 definition, then we are not relying on the absolute flux prediction, and only doing a relative rate analysis between ADs. This is the default analysis mode. Table 20 provides a summary of the parameters $\boldsymbol{\theta}$ in this physical model. By default, all parameters except for θ_{13} and δ^{corr} are constrained by penalty terms. There are a total of 2 *free parameters* and 21 *nuisance parameters* in this model.

Table 20. Summary of Model Parameters in Rate-only Analysis

Parameter	Description	Count
$\sin^2(2\theta_{13})$	Short-baseline neutrino oscillation amplitude parameter	1
δ^{corr}	Total correlated variation in the expected $\bar{\nu}_e$ event rate	1
Δm_{13}^2	Short-baseline neutrino oscillation frequency parameter	1
$\sin^2(2\theta_{12})$	Long-baseline neutrino oscillation amplitude parameter	1
Δm_{12}^2	Long-baseline neutrino oscillation frequency parameter	1
δ_j^{AD}	Uncorrelated rate variation between each detector j	6
δ_k^r	Uncorrelated flux variation between each reactor k	6
δ_j^b	Uncorrelated rate variation in backgrounds in detector j	6

4.2 Best Fit Parameters

(The reactor flux is unblinded on Feb 29th, 2010.)

Fig 17(a) shows the ratio of measured $\bar{\nu}_e$ events over expected events at each detector, assuming no oscillation. The x-axis shows the baseline of each detector weighted by the flux from each core. The 3 far site detectors are artificially separated by ± 50 meter to make them distinguishable on the figure. The grey band indicates the correlated uncertainty on total rate prediction, which is made a free parameter in the model. The error bars are statistical only. Large deficit is obvious at the far detectors relative to the near detectors. Fig 17(b) shows the ratio of measured $\bar{\nu}_e$ events over expected events at the best fit model parameters. The uncorrelated flux variation between each reactor δ_k^r (Table 20) is enlarged to 10% to account for the blinded power variations. The best fit parameters are summarized in Table. 21. The uncertainties on the best fit parameters are directly from the Minuit fitter. The goodness of fit is $\chi_{min}^2/\text{ndf} = 1.85/4.$, a p-value of 0.76.

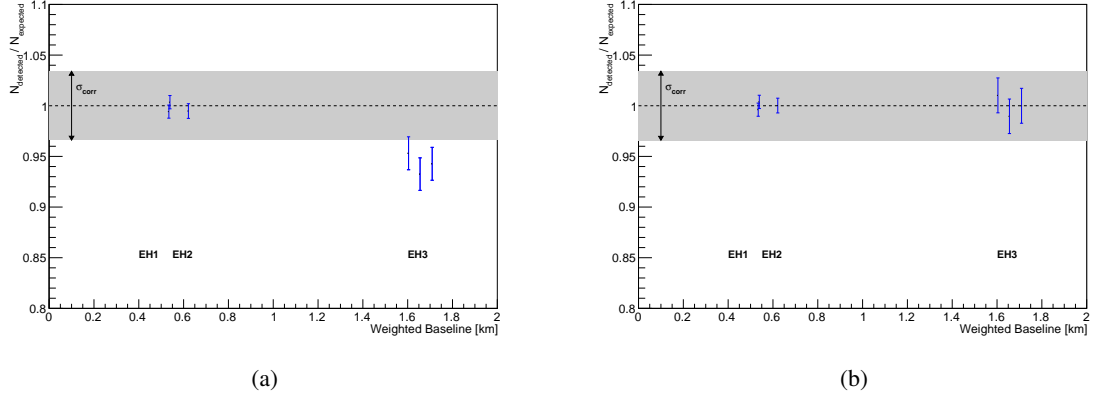


Figure 17. (a) The ratio of measured $\bar{\nu}_e$ events over expected events at each detector, assuming no oscillation. The x-axis shows the baseline of each detector weighted by the flux from each core. The 3 far site detectors are artificially separated by ± 50 meter to make them distinguishable on the figure. The grey band indicates the correlated uncertainty on total rate prediction, which is made a free parameter in the model. The error bars are statistical only. Large deficit is obvious at the far detectors relative to the near detectors. (b) The ratio of measured $\bar{\nu}_e$ events over expected events at the best fit model parameters. The goodness of fit is $\chi^2_{\min}/\text{ndf} = 1.85/4$, a p-value of 0.76.

Table 21. Best Fit Parameters. For nuisance parameters, the uncertainties are not shown.

$\sin^2(2\theta_{13})$	0.0931 ± 0.0180					
δ^{corr}	0.014 ± 0.011					
Δm_{13}^2	$2.43\text{e-}3$					
$\sin^2(2\theta_{12})$	0.861					
Δm_{12}^2	$7.59\text{e-}5$					
	1	2	3	4	5	6
$\delta_j^{AD} [\%]$	0.08	-0.09	0.03	0.03	-0.03	-8e-5
$\delta_k^r [\%]$	-0.07	-0.05	0.03	0.02	0.03	0.04
$\delta_j^b [\%]$	0.56	-0.56	0.07	0.60	-0.60	-0.003

4.3 Results on Theta13

Fig. 18 shows the 1-D scan of the χ^2 distribution of $\sin^2 2\theta_{13}$, by marginalize all other parameters. The $\chi^2_{\min}/\text{ndf} = 1.85/4$, corresponding to p-value of 0.76. From the line corresponding to $\Delta\chi^2 = 1$ we find:

$$\sin^2 2\theta_{13} = 0.093^{+0.018}_{-0.018} \quad (4.8)$$

The significance of $\sin^2 2\theta_{13} > 0$ is 5.1σ , or 99.99998% C.L.

Fig 19 shows how the significance of $\sin^2 2\theta_{13} > 0$ depends on the size of AD relative uncertainty and reactor uncorrelated uncertainty. θ_{13} result is quite in-sensitive to the core-to-core variation, largely due to the cancelation effects between near/far detectors. On the other hand, θ_{13} result is quite sensitive the AD relative uncertainty, which needs to be carefully accessed and controlled. The design principles of identical detectors cannot be more stressed.

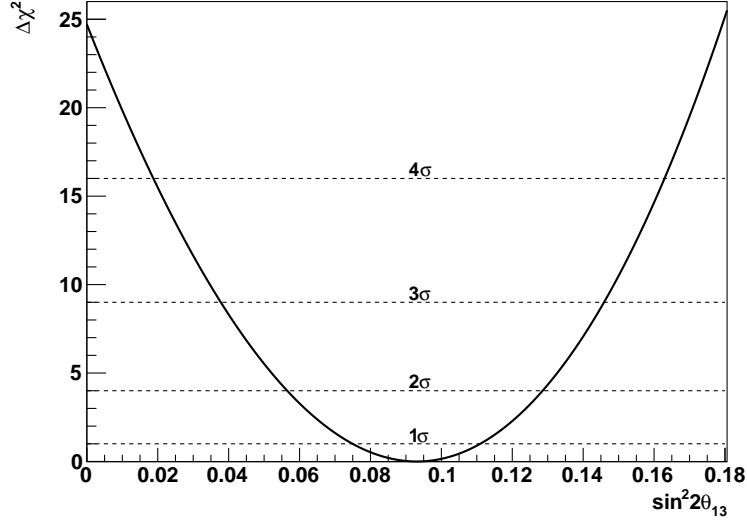
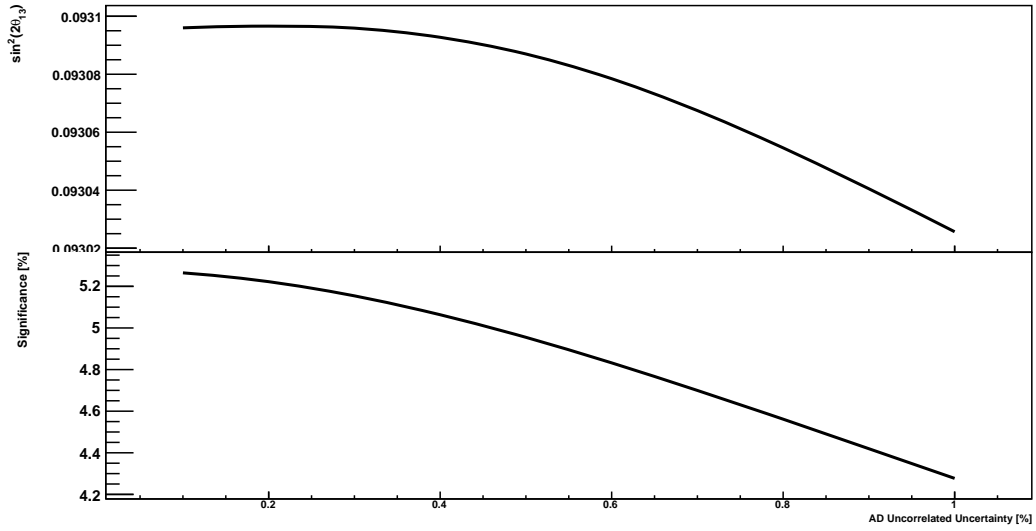
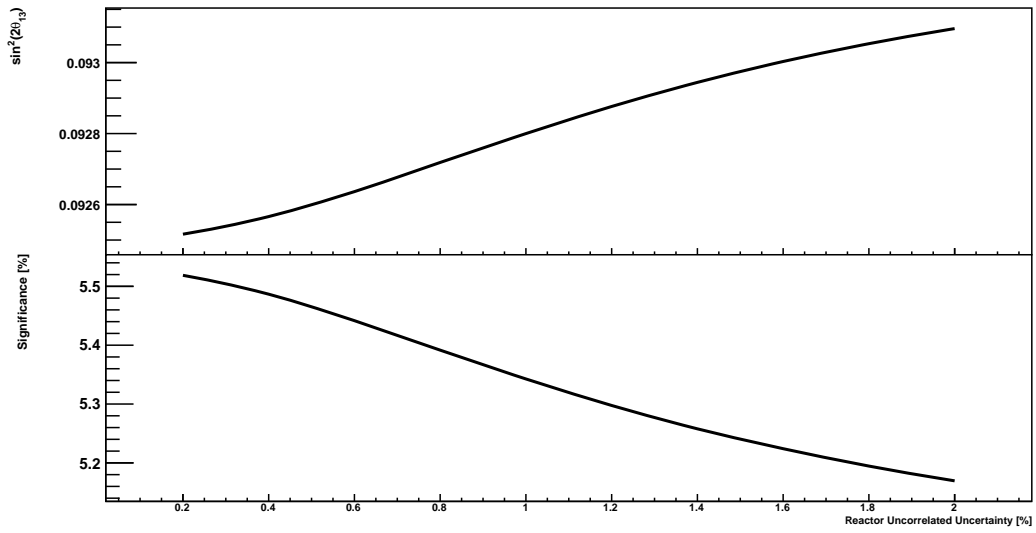


Figure 18. χ^2 distribution of $\sin^2 2\theta_{13}$.

Finally, Fig. 20 shows the 2-D χ^2 contours of Δm_{31}^2 vs. $\sin^2 2\theta_{13}$. In Fig. 20(a) Δm_{31}^2 is not constrained. The rate only analysis is quite insensitive to the Δm_{31}^2 . As we collect more statistics, the spectra distortion at the far detectors will have some sensitivity on the Δm_{31}^2 . In Fig. 20(a) Δm_{31}^2 is constrained by global Δm_{32}^2 measurements ($\Delta m_{32}^2 = (2.43 \pm 0.13) \times 10^{-3} eV^2$), mainly from the MINOS disappearance results.

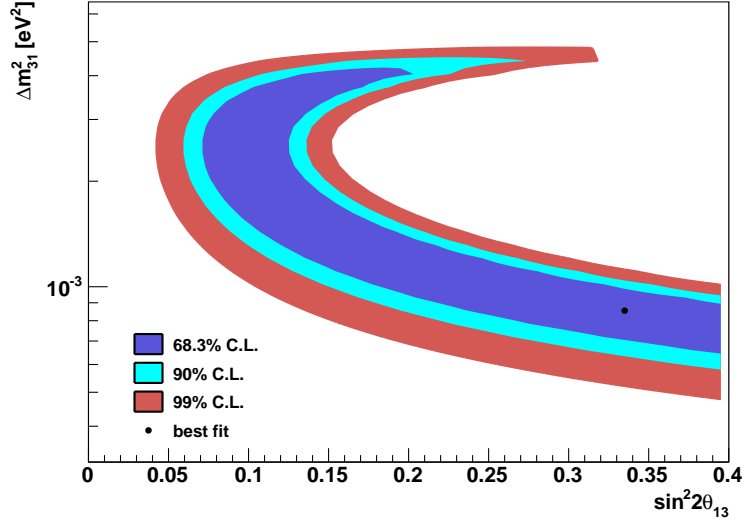


(a)

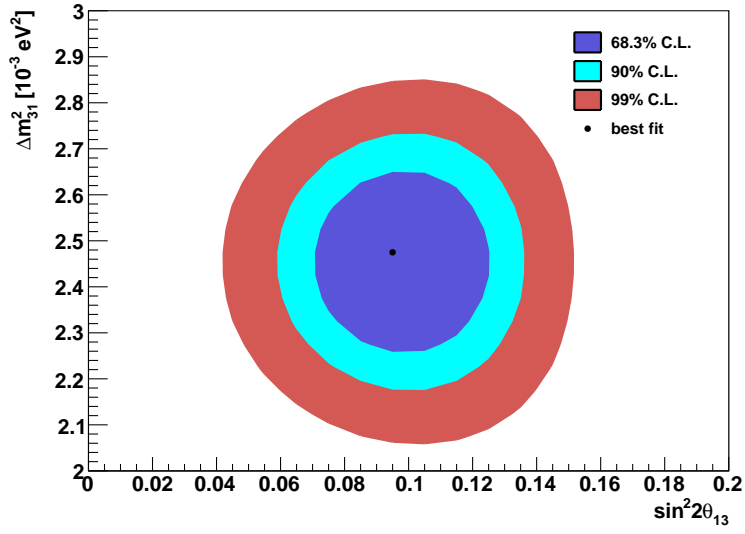


(b)

Figure 19. The central value of $\sin^2 2\theta_{13}$ and significance of $\sin^2 2\theta_{13} > 0$ as a function of the (a) AD relative uncertainty (b) reactor relative uncertainty.



(a)



(b)

Figure 20. The 2-D χ^2 contours of Δm^2_{31} vs. $\sin^2 2\theta_{13}$ (a) with only the Daya Bay experiment data; (b) constrained by global Δm^2_{32} measurements.

Acknowledgments

We thank CWG / PWG / DQWG for providing the the consistent sets of data, without which this analysis won't be possible. We thank all the fruitful discussions and suggestions from our collaborators.

References

- [1] Data Quality Check (doc:7464), *Gaosong Li et al.*
- [2] AdSimple Reconstruction (doc:7334), *Yasuhiro Nakajima et al.*
- [3] Trigger Efficiency Study (doc:7499), *Weili Zhong et al.*
- [4] Absolute IBD Efficiency from MC (doc:7548), *Chao Zhang et al.*
- [5] Absolute IBD Efficiency from MC (doc:7686), *Guofu Cao et al.*
- [6] Energy Scale Study (doc:7518), *Xin Qian et al.*
- [7] Energy Scale Uncertainty Study (doc:7682), *Xin Qian et al.*
- [8] AdSimple Energy Scale Uncertainty (doc:7583), *Yasuhiro Nakajima et al.*
- [9] Understanding Gd Capture Time (doc:7299), *Xin Qian et al.*
- [10] Neutron Capture Time Comparison (doc:7672), *Jiajie Ling et al.*
- [11] Summary of Flasher ID Algorithms (doc:7434), *Wei Wang et al.*
- [12] Flasher Efficiency Study (doc:7677), *Xin Qian et al.*
- [13] Correlated Flasher Background Study (doc:7537), *Xin Qian et al.*
- [14] Singles Rate Investigation (doc:7466), *Xin Qian et al.*
- [15] Accidental Background Study (doc:7679), *Fenfang Wu et al.*
- [16] Neutron-like Singles Study (doc:7043), *Liangjian Wen et al.*
- [17] Simulation on AmC Background (doc:6779), *Wenqiang Gu et al.*
- [18] Estimation of AmC Background (doc:7568), *Fenfang Wu et al.*
- [19] Discussions of Event Time distribution (doc:7278), *Xin Qian et al.*
- [20] Estimation of (α ,n) Background (doc:7509), *Zeyuan Yu et al.*
- [21] AD 1/2 Liquid Property (doc:6615), *Minfang Yeh et al.*
- [22] Li9/He8 Background Study (doc:7653), *Jiajie Ling et al.*
- [23] IBD Analysis TechNote (doc:7508), *Liangjian Wen et al.*
- [24] Fast Neutron Background Study (doc:7539), *Jiajie Ling et al.*
- [25] Study Fast Neutron Background with RPC (doc:7538), *Xin Qian et al.*
- [26] <http://www.nndc.bnl.gov/exfor/endf00.jsp>
- [27] Side-by-side comparison of Daya Bay Antineutrino Detectors, *to be published*
- [28] *Z. Djurcic et al. J. Phys. G. 36, 045002 (2009).*

- [29] *Hahn, A.A. et al.* Phys. Lett. B **218** (1989) 365.
- [30] *K. Schreckenbach. et al.* Phys. Lett. B **160** (1985) 325.
- [31] *P. Vogel et al.* Phys. Rev. C **24** (Oct, 1981) 1543–1553.
- [32] *P. Vogel et al.* Phys. Rev. D **60** (Jul, 1999) 053003.
- [33] *D. Wilkinson* Nuclear Physics A **377** (1982), no. 2-3, 474 – 504.
- [34] *P. Vogel* Phys. Rev. D **29** (May, 1984) 1918–1922.
- [35] *K. Nakamura et al.* J. Phys. G. **37**, 075021 (2010).